

**BUILDING A TENSEGRITY-BASED COMPUTATIONAL  
MODEL TO UNDERSTAND ENDOTHELIAL ALIGNMENT  
UNDER FLOW**

by

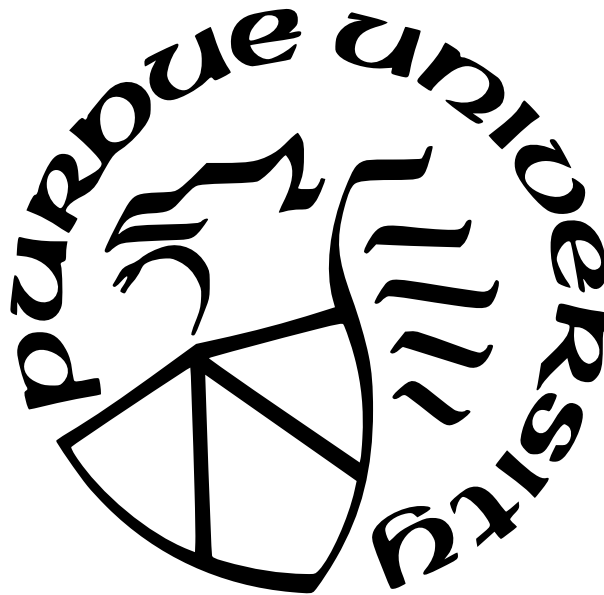
**Tamara Al-Muhtaseb**

**A Thesis**

*Submitted to the Faculty of Purdue University*

*In Partial Fulfillment of the Requirements for the degree of*

**Master of Science in Biomedical Engineering**



Department of Biomedical Engineering

Indianapolis, Indiana

December 2021

**THE PURDUE UNIVERSITY GRADUATE SCHOOL  
STATEMENT OF COMMITTEE APPROVAL**

**Dr. Julie Ji, Chair**

Department of Biomedical Engineering

**Dr. Sungsoo Na**

Department of Biomedical Engineering

**Dr. Andres Tovar**

Department of Mechanical and Energy Engineering

**Approved by:**

Dr. Joseph Wallace

## ACKNOWLEDGMENTS

First and foremost, I am forever grateful for Allah for the opportunity that got me here. My journey started really rough but I believe it was what I needed to grow and learn to explore my own path.

My sincere appreciation goes to my advisor, Dr. Julie Ji, for welcoming me into her lab and for guiding me and spending time on my research. I would also like to thank my advisory committee members, Dr. Andres Tovar and Dr. Sungsoo Na, for their time and support throughout my thesis.

For my lovely mother and my forever best-friend. I know how hard it was for you to let me travel and live far away from you. Thank you for supporting my decision to pursue a different future and for being my number one encourager.

My deepest gratitude goes to my lab member, Yizhi Jiang, for teaching and helping me with all the experimental work. Thank you for being patient with me and answering all my questions even the ones I keep repeating.

Finally, for my family and friends, who have been with me every step of the way, thank you for being the best supporters and I hope that one day I can be there for you as you have been for me.

# TABLE OF CONTENTS

LIST OF TABLES . . . . .	7
LIST OF FIGURES . . . . .	8
ABSTRACT . . . . .	11
1 INTRODUCTION . . . . .	12
1.1 Endothelial Cells Under Mechanical Forces . . . . .	12
1.2 Mechanotransduction in Endothelial Cells . . . . .	13
1.3 Microtubule-Organizing Center (MTOC) and Nuclear Orientation . . . . .	14
1.4 Hutchinson-Gilford Progeria Syndrome (HGPS) . . . . .	15
1.5 Thesis Objectives . . . . .	18
2 COMPUTATIONAL MODELING . . . . .	19
2.1 Cell Biology . . . . .	19
2.1.1 Plasma Membrane . . . . .	20
2.1.2 Nucleus . . . . .	20
2.1.3 Cytoplasm . . . . .	20
2.1.4 Cytoskeleton . . . . .	20
2.2 Continuum-Tensegrity Cell Modeling . . . . .	21
2.2.1 Summary of Literature Review . . . . .	22
2.2.2 Continuum Model . . . . .	26
2.2.3 Tensegrity Model . . . . .	28

2.3	Fluid Modeling . . . . .	30
2.4	Model Analysis . . . . .	30
2.5	Results . . . . .	32
2.6	Discussion and Limitations . . . . .	34
3	EXPERIMENTAL . . . . .	37
3.1	Methods . . . . .	37
3.1.1	Cell Culture . . . . .	37
3.1.2	Shear Stress Experiment . . . . .	38
3.1.3	Immunofluorescence . . . . .	41
3.1.4	Image Analysis of the Nucleus and MTOC . . . . .	42
3.1.5	Statistical Analysis . . . . .	43
3.2	Results . . . . .	44
3.2.1	MTOC-Nuclear Orientation Angle is Opposite Between Wild-Type and Progerin Cells in Vertical Wound Upstream and Downstream of Flow . . . . .	44
3.2.2	Classified Positioning of MTOC Show Different Response to Flow at The Vertical Wound Edge Between Wild-Type and Progerin Cells . . . .	48
3.3	Discussion . . . . .	51
4	CONCLUSIONS AND SUMMARY . . . . .	53
4.1	Conclusions . . . . .	53
4.2	Future Work . . . . .	53

LIST OF REFERENCES . . . . . 55

## LIST OF TABLES

- 2.1 Mechanical properties used for the continuum part of the finite element model. . . 27
- 2.2 Mechanical properties used for the tensegrity part of the finite element model. . . 29

## LIST OF FIGURES

1.1	Schematic diagram showing different types of mechanical forces acting on the endothelium due to blood flow. The shear stress is parallel to the endothelial cell surface, the normal stress is perpendicular to the endothelial cell surface and the circumferential stretch is due to the action of pressure [8]. . . . .	13
1.2	Schematic drawing of typical lamins structures: (A) Includes N-terminal head, $\alpha$ -helix rod domain, a C-terminal tail that contains NLS (nuclear localization signal) and Ig fold domain. (B) Post-translational changes: (a) Lamins after protein synthesis contain a complete -CAAX motif at C-terminus, (b) The cysteine in -CAAX motif is farnesylated by FTase. (c) The aaX residues are removed and the cysteine at the C-terminus is methylated. (d) The last 15 amino acids are removed by ZMPSTE24 and mature lamin A is generated [32]. . . . .	16
1.3	Nuclei of a normal cell and progeria cell [33]. . . . .	17
1.4	(A) Anticipated orientation of the nucleus and MTOC in confluent healthy endothelial cells under shear stress. MTOC is upstream of nucleus (red arrows). (B) At the wound edge, MTOC is reoriented to a position between the leading edge and the nucleus. . . . .	18
2.1	Eukaryotic cell [37]. . . . .	19
2.2	Cytoskeletal components and their structure: microtubules (green), actin filaments (red), and intermediate filaments (blue) [45]. . . . .	21
2.3	Tensegrity model consisting of 6 struts and 24 cables. (A) Round. (B) Spread configurations. [50] . . . . .	22
2.4	Tensegrity model consisting of 6 microtubule struts (AA, BB and CC), 24 actin filament cables (AB, AC and BC) and 12 intermediate filament radial cables (OA, OB and OC) [51]. . . . .	23
2.5	Finite element models (a) to (b) of adherent cells at increasingly spread configurations consisting of nucleus, plasma membrane, cytoplasm and cytoskeleton tensegrity structure of microtubules (dark/red lines) and actin filaments (light/blue lines) [46]. . . . .	24
2.6	Finite element model of suspended cell: (a) Continuum section. (b) Tensegrity section [47]. . . . .	25
2.7	Finite element model of a single cell. (A) Microtubules. (B) Actin bundles. (C) Actin bundles and microtubules with respect to the nucleus [52]. . . . .	25
2.8	A three-dimensional cell model in a sliced view to allow the visualization of the internal components: microtubules (blue), cytoplasm (green), plasma membrane (yellow), glass substrate (gray), and nucleus (orange). . . . .	26
2.9	Microscopic image of endothelial cells. . . . .	28

2.10	(A) Tensegrity part of the hybrid model includes 6 microtubules (blue) and 24 actin filaments (red). (B) A sliced view of the hybrid model to show the internal components: microtubules (blue), actin filaments (red), nucleus (purple), cytoplasm (green), and plasma membrane (dark blue). (C) A full view of the cell model with the tensegrity part inside. . . . .	29
2.11	(A) Dimensions of the flow channel. (B) Meshing of the flow channel. . . . .	30
2.12	Pressure imported from the fluid analysis onto the plasma membrane. . . . .	31
2.13	Meshing of the cell model. . . . .	32
2.14	High distortion error message in Ansys Workbench. . . . .	32
2.15	Internal solution magnitude error message in Ansys Workbench. . . . .	33
2.16	Total Deformation of the simple geometry model created. . . . .	34
2.17	First attempt of a computational cell model designed in NX. . . . .	35
2.18	Second attempt of a computational cell model designed in Creo. . . . .	35
3.1	Setup of shear stress system: (A) Components of parallel- plate flow chamber. (B) Housing environment [56]. . . . .	39
3.2	Fluid flow profile for the parallel-plate flow chamber. . . . .	40
3.3	(A) MTOC-nuclear orientation as an angle ranging from 0 to 180 degrees. 0 means that MTOC was located downstream of the shear direction and the nucleus, while 180 means that MTOC was located upstream of the shear direction and the nucleus. (B) Categorized distribution of MTOC-nuclear orientation. MTOCs were grouped as downstream of the nucleus (scored 1), downstream of the midpoint of the nucleus (scored 2), and upstream of the midpoint of the nucleus (scored 3), and cells upstream of the nucleus (scored 4). . . . .	43
3.4	The average of MTOC-nuclear orientation angle (ranges from 0 to 180 degrees) in wild-type and progerin-expressing BAECs under static and sheared conditions. 0° means that MTOC was located downstream of the shear direction as to the nucleus, while 180° means that MTOC was located upstream of the shear direction as to the nucleus. The full region represents the area away from wounds, the vertical region is the area near the vertical wound and the horizontal region is the area near the horizontal wound. (A) Wild-type and progerin-expressing cells under static conditions. (* P = 0.05, wild-type vs. progerin cells) (B) Wild-type and progerin-expressing cells after 4 hours of shear stress. (# P = 0.07 static vs. sheared progerin cells , * * P = 0.08, wild-type vs. progerin cells). . . . .	46

3.5	Representative images of wild-type and progerin-expressing BAECs labeled for nuclei and MTOC under static and sheared conditions. (A) Wild-type cells under static conditions. (B) Progerin-expressing cells under static conditions. (C) Wild-type cells after 4 hours of shear stress. (D) Progerin-expressing cells after 4 hours of shear stress. Cells from left to right were shown: stained for nuclei with Hoechst, stained for MTOC with anti- $\gamma$ -tubulin conjugated with Alexa Flour 594, and overlay of both stains. Scale bar - 25 $\mu$ m . . . . .	47
3.6	Categorized distribution of MTOC-nuclear orientation in wild-type and progerin-expressing BAECs in static and sheared conditions. The downstream here is class 2 including class 1. While the upstream is class 3 including class 4. The full region represents the area away from wounds, the vertical region is the area near the vertical wound and the horizontal region is the area near the horizontal wound. (A) Wild-type cells under static conditions. (B) Progerin-expressing cells under static conditions. (C) Wild-type cells after 4 hours of shear stress. (D) Progerin-expressing cells after 4 hours of shear stress. . . . .	49
3.7	Categorized distribution of MTOC-nuclear orientation in wild-type and progerin-expressing BAECs in static and sheared conditions. Group A is downstream of the nucleus, group B is downstream of the midpoint of the nucleus, group C is upstream of the midpoint of the nucleus, and Group D is upstream of the nucleus. The full region represents the area away from wounds, the vertical region is the area near the vertical wound and the horizontal region is the area near the horizontal wound. (A) Wild-type cells under static conditions. (B) Progerin-expressing cells under static conditions. (C) Wild-type cells after 4 hours of shear stress. (D) Progerin-expressing cells after 4 hours of shear stress. . . . .	50

## ABSTRACT

Endothelial cells form the lining of the walls of blood vessels and are continuously subjected to mechanical stimuli from the blood flow. Microtubule-organizing center (MTOC), also known as centrosome is a structure found in eukaryotic cells close to the nucleus. MTOC relocates relative to the nucleus when endothelial cells are exposed to shear stress which determines their polarization, thus it plays a critical role in cell migration and wound healing. The nuclear lamina, a mesh-like network that lies underneath the nuclear membrane, is composed of lamins, type V intermediate filament proteins. Mutations in LMNA gene that encodes A-type lamins cause the production of a mutant form of lamin A called progerin and leads to a rare premature aging disease known as Hutchinson-Gilford Progeria Syndrome (HGPS). The goal of this study is to investigate how fluid flow affects the cytoskeleton of endothelial cells.

This thesis consists of two main sections; computational mechanical modeling and laboratory experimental work. The mechanical model was implemented using Ansys Workbench software as a tensegrity-based cellular model in order to simulate the state of an endothelial cell under the effects of induced shear stress from the blood fluid flow. This tensegrity-based cellular model - composed of a plasma membrane, cytoplasm, nucleus, microtubules, and actin filaments - aims to understand the effects of the fluid flow on the mechanics of the cytoskeleton. In addition, the laboratory experiments conducted in this study examined the MTOC-nuclear orientation of endothelial cells under shear stress with the presence of wound healing. Wild-type lamin A and progerin-expressing BAECs were studied under static and sheared conditions.

Moreover, a custom MATLAB code was utilized to measure the MTOC-nuclear orientation angle and classification. Results demonstrate that shear stress leads to different responses of the MTOC orientation between the wild-type and progerin-expressing cells around the vertical wound edge. Future directions for this study involve additional experimental work together with the improved simulation results to confirm the MTOC orientation relative to the nucleus under shear stress.

# 1. INTRODUCTION

In this chapter endothelial cells are introduced and their mechanobiology and mechanotransduction phenomena are described. This is followed by an explanation of the cellular polarization concept and the role of the microtubule-organizing center and nuclear orientation. Furthermore, nuclear lamins and their relations to Hutchinson-Gilford Progeria Syndrome (HGPS) will be detailed. Finally, the thesis objectives will be presented.

## 1.1 Endothelial Cells Under Mechanical Forces

Blood vessels (arteries, veins, and capillaries) are made up of three main layers, an inner layer (tunica intima), a middle layer (tunica media), and an external layer (tunica adventitia) [1, 2]. The tunica intima includes a monolayer of endothelial cells (ECs) and the internal elastic lamina [1]. ECs, which line up the inside wall of the blood vessel and form the endothelium tissue, have crucial roles in various physiological processes for instance coagulation, angiogenesis, blood flow regulation, and inflammation [3, 4]. The tunica media is mainly composed of smooth muscle cells (SMCs) collagen fibers and fibroplastic elements [1]. Blood flow is established by the contraction-relaxation of SMCs [4]. The tunica adventitia is a complex layer that contains different cell types such as macrophages, lymphocytes, dendritic cells, and fibroblasts as well as perivascular nerves. It facilitates interactions within SMCs and ECs and their local tissue environment [5].

The flow of blood in arteries subjects the endothelium to different types of mechanical forces as shown in Figure 1.1. These forces include normal hydrostatic pressure, cyclic tensile stretch, and tangential fluid shear stress [6–9].

The hemodynamic fluid-wall shear stress (WSS), is interpreted as the frictional force component per unit area, caused by the flow of blood inflicted on the inner surface of the blood vessels. This shear stress is mostly endured by the monolayer of ECs, which is exposed directly to the blood flow [8, 10, 11].

From literature, the value of WSS in veins is estimated to range from 1 to 6  $dyn/cm^2$ , whereas in arteries it is between 10 and 70  $dyn/cm^2$  [8, 10]. In chapter 3 of this thesis, the mechanics of fluid flow will be further explained for *in vitro* experiments.

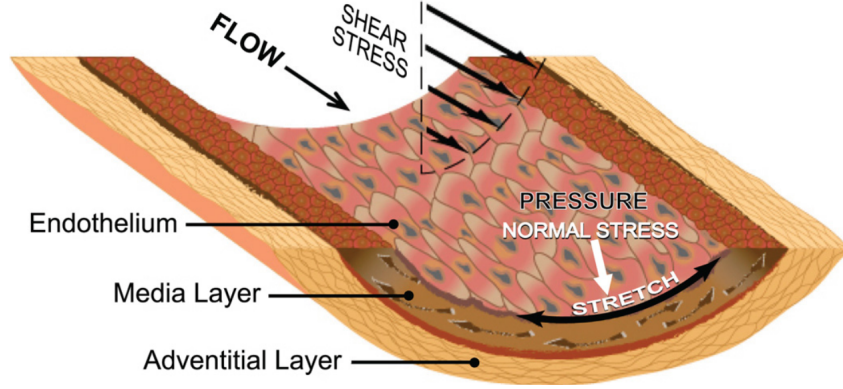


**Figure 1.1.** Schematic diagram showing different types of mechanical forces acting on the endothelium due to blood flow. The shear stress is parallel to the endothelial cell surface, the normal stress is perpendicular to the endothelial cell surface and the circumferential stretch is due to the action of pressure [8].

Shear stress can be recreated in an experimental setup using a parallel plate flow chamber. In a flow chamber, the wall shear stress,  $\tau_w$ , for fluids can be calculated using Equation 1.1, where  $\mu$  is the dynamic viscosity of the fluid,  $u$  is the fluid velocity along the boundary, and  $y$  is the height above the boundary [11]:

$$\tau_w = \mu \frac{du}{dy} \quad (1.1)$$

The WSS for blood flowing in vessels is also defined by the Hagen-Poiseuille equation as shown in Equation 1.2, where  $Q$  is the volumetric flow rate of the blood and  $r$  is the inner radius of the blood vessel [11]:

$$\tau_w = 4\mu \left( \frac{Q}{\pi r^3} \right) \quad (1.2)$$

## 1.2 Mechanotransduction in Endothelial Cells

As stated in the previous section, endothelial cells are constantly exposed to different mechanical stimuli. ECs sense the mechanical force physically and convey it into a biochemical signal through a process called mechanotransduction [12]. Disturbed blood flow causes different responses in ECs compared to steady laminar flow. Disturbance in the blood flow is commonly observed within sites of vessel curvature and branching. Such flow initiates

proinflammatory and apoptotic signaling in ECs which, in turn, leads to endothelial dysfunction. This dysfunction is the primary cause for the development of atherosclerosis, a cardiovascular disease where plaques build up in the arterial wall [13].

*In vivo* research indicates that endothelial morphologies are related to their local mechanical surrounding. The endothelial cell orientation correlates with blood flow directions [14]. In areas where the flow is non-uniform particularly at the aorta, this orientation seems less organized [15]. EC remodeling due to mechanical forces contributes in maintaining the endothelial homeostasis, whereas a disturbance can affect this balance and initiate atheroprone at the local site [16]. Mechanical forces applied on cells initiate mechanosensitive pathways that lead them to adjust their structure through the cytoskeleton [15]. Moreover, *in vitro* studies showed that when endothelial cells are exposed to different mechanical forces, they respond by changing their morphology. With shear stress, flow patterns regulate the EC morphological responses. With sustained steady laminar shear stress of high amplitudes (greater than  $12 \text{ dyn/cm}^2$ ), microtubules and actin filaments aligned with the flow direction, and an intact microtubule network was necessary for the cell morphology changes [17]. In contrast, when oscillatory flow or laminar shear stress of low magnitude (less than  $5 \text{ dyn/cm}^2$ ) was applied to ECs, they maintained their shape [15].

Maintaining an intact endothelium is vital to a healthy vasculature, and improper arterial wall healing in response to injury contributes to the development of atherosclerosis. When the endothelium is disrupted, it will trigger the activation of ECs to begin repair through wound healing. Mechanotransduction plays a critical role in endothelial cell migration and vascular wound healing considering the hemodynamic surrounding of the endothelium [18].

### **1.3 Microtubule-Organizing Center (MTOC) and Nuclear Orientation**

Microtubules are cytoskeleton filaments that emerge from the microtubule-organizing center (MTOC) which is a structure found near the nucleus of eukaryotic cells. Cellular polarization is a vital trait established by various cell types and plays a critical role in cell migration, cell differentiation, wound healing, and other organ functions. For the cell to be polarized, the cell's nucleus will be observed on one side, whereas the MTOC and the Golgi

apparatus will be on the opposite side [19, 20]. Therefore, the MTOC's location in relation to the nucleus is what regulates cellular polarization [21].

Directional cell migration, defined as when cells move from a certain location to the next, is very crucial for wound healing, immune functions and development. To achieve this, the MTOC will relocate to be within the nucleus and the leading edge of the cell, which allows the microtubules to grow towards the leading edge [21–23]. To examine cellular polarization *in vitro*, it is common to use the scratch-wound assay where a confluent monolayer of cells are grown, then a scratch is created to form an empty area without any cells. The cells will then be studied during migration towards the wound area [21].

Furthermore, shear stress from blood flow causes planer cell polarity in endothelium [19]. In the arteries, the MTOC is reoriented upstream of the nucleus, whereas in veins the MTOC is downstream of the nucleus. Thus, cellular polarization in the endothelium is determined by the direction of the shear stress [24].

In a previous *in vitro* study, human aortic endothelial cells (HAEC) were examined under  $15 \text{ dyn/cm}^2$  shear stress, and it was illustrated that MTOC polarized upstream of the nucleus. Nesprin-3, a nuclear-cytoskeleton linking protein was found to be responsible for the MTOC-nuclear orientation under fluid flow [25].

#### 1.4 Hutchinson-Gilford Progeria Syndrome (HGPS)

The nuclear lamina is a mesh resembling network of proteins that lies underneath the nuclear membrane. It provides mechanical support to the nucleus of the cell. It is also essential for chromatin organization and transcription regulation at the nuclear periphery. The lamina is responsible for signal transduction as it is located between the nucleus and the cytoskeleton of the cell [26, 27].

Lamins are type V intermediate filament proteins and the primary components of the nuclear lamina [27]. They are divided into two types: A-type and B-type. The former is established by the alternative splicing of the LMNA gene and includes lamins A, C, A $\Delta$ 10 and C2, while the latter consist of lamins B1, B2, and B3 formed by LMNB1 and alternative splicing of the LMNB2 gene [28].

Hutchinson Gilford Progeria Syndrome (HGPS), a premature aging disease that causes children prior to their teenage years to develop various symptoms including hair loss, bone and joint abnormalities, scleroderma, and atherosclerosis [29, 30]. Despite the rarity of HGPS, affecting 1 in 4–8 million children, researchers continue to be interested in studying it after discovering that a gene mutation drives its pathophysiology [29, 31].

A de novo mutation of the LMNA gene triggers the production of a mutant form of prelamin A called progerin. This mutation is the main cause of HGPS. The average age of death for HGPS patients is 14.6 years, mainly due to a stroke or myocardial infarction that resulted from the rapid progress of atherosclerosis [30].

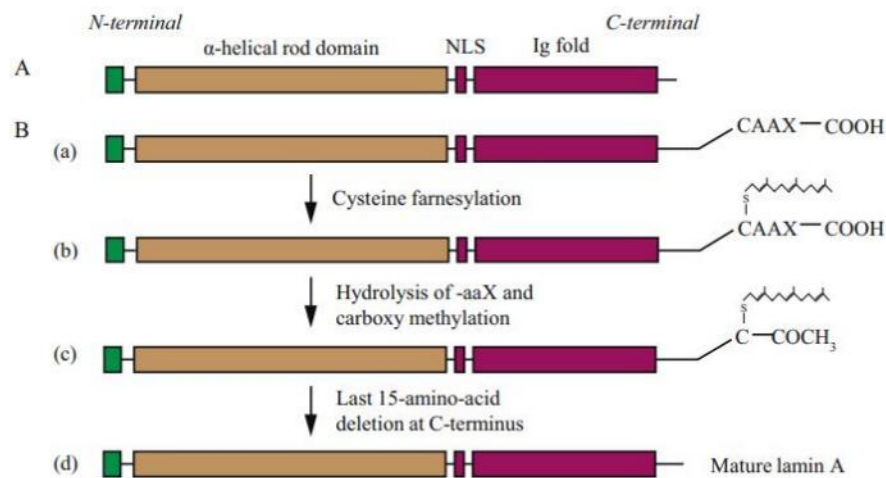


**Figure 1.2.** Schematic drawing of typical lamins structures: (A) Includes N-terminal head,  $\alpha$ -helix rod domain, a C-terminal tail that contains NLS (nuclear localization signal) and Ig fold domain. (B) Post-translational changes: (a) Lamins after protein synthesis contain a complete –CAAX motif at C-terminus, (b) The cysteine in –CAAX motif is farnesylated by FTase. (c) The aaX residues are removed and the cysteine at the C-terminus is methylated. (d) The last 15 amino acids are removed by ZMPSTE24 and mature lamin A is generated [32].

As previously discussed A-type lamins especially lamins A and C are produced from the alternative gene splicing of LMNA. The useful form of lamin C is generated in a direct way, while lamin A follows a more complicated path. The prelamin A, precursor form, is generated and next goes through a sequence of post-translational changes. First, methylation and

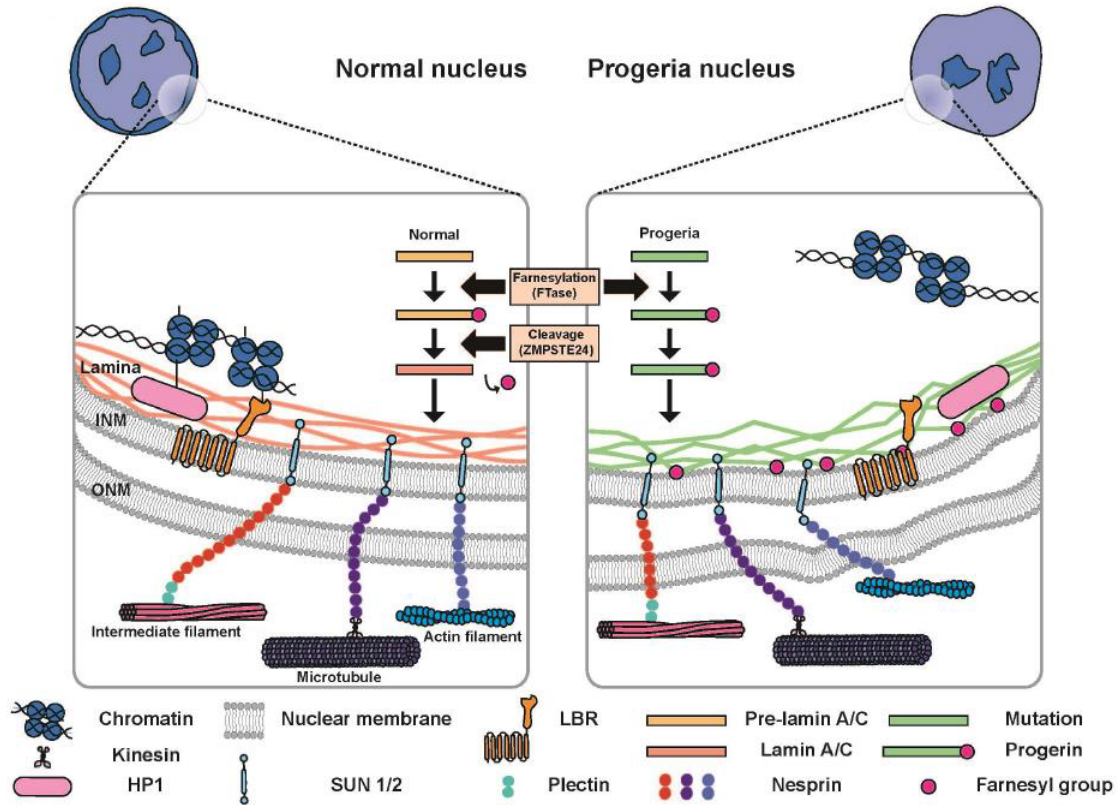


**Figure 1.3.** Nuclei of a normal cell and progeria cell [33].

farnesylation of the prelamin A where cholesterol production will derive lipid intermediates that can be added to the C tail of the protein. Farnesyltransferase (FTase) is the catalyst of this reaction. Next, zinc metalloprotease ZMPSTE24 will assist the cleavage steps that will take place two times where the remains of methyl and farnesyl groups and the 15 tail of amino acids are removed. After that, the mature form of lamin A is completed and functional as shown in Figure 1.2. In HPGS, the before-mentioned process is compromised and the final cleavage step is skipped and progerin is generated instead [32–34].

Figure 1.3 illustrates how normal vs. progerin lamins are incorporated into the nuclear lamina. Nuclei from HPGS cells are mechanically less stable than that of normal cells because of the adjusted lamina composition. In addition, the accumulation of progerin, the mutant form of lamin A, in the nuclear envelope promotes changes in the shape and structure of the nucleus, increases the thickness of the lamina, causes the chromatin detachment from the nuclear envelope, and will increase the sensitivity to mechanical strain [30, 33].

## 1.5 Thesis Objectives

Section 1.1 demonstrated that when confluent endothelial cells are exposed to fluid flow, the MTOC reorient to be upstream of the nucleus as shown in Figure 1.4A. However, during cell migration and wound healing, the MTOC relocates to be between the leading edge and the nucleus [21–23]. In this thesis, we will begin to address the question:

Does shear stress in the presence of a wound influence the orientation of the MTOC relative to the nucleus?

We hypothesize that cytoskeleton re-orient and re-organize to minimize forces on the nucleus. It is hypothesized that the MTOC might re-orient from upstream of the nucleus to downstream of the nucleus when the cell is exposed to fluid flow during wound healing, as shown in Figure 1.4B. This orientation may also vary between the up and down wound edges.

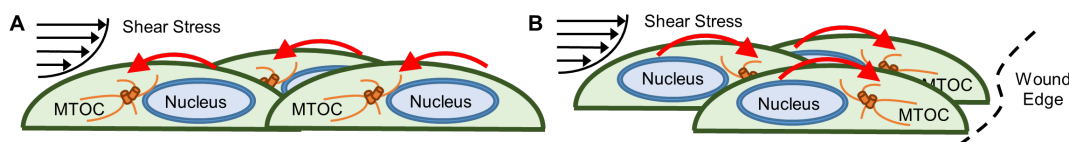


**Figure 1.4.** (A) Anticipated orientation of the nucleus and MTOC in confluent healthy endothelial cells under shear stress. MTOC is upstream of nucleus (red arrows). (B) At the wound edge, MTOC is reoriented to a position between the leading edge and the nucleus.

To achieve this goal, there are two main parts of this thesis project. The first part is composed of building a hybrid computational mechanical model of an endothelial cell. The purpose of the model is to simulate a physical endothelial cell represented as a tensegrity and continuum structure in order to examine the mechanics of the cell in response to blood-like fluid flow.

The second part consists of *in vitro* experiments conducted to investigate the MTOC-nuclear orientation under fluid flow. We will also compare endothelial cells expressing wild-type lamin with cells expressing the mutant form progerin, to evaluate the effect of progerin in cell nucleus-MTOC positioning.

## 2. COMPUTATIONAL MODELING

This chapter commences with a background on cell biology describing the structure and functions of different cell components. The following section summarizes mechanical models from literature and discusses the continuum and the tensegrity part of the cell model created. Furthermore, the fluid domain and the analysis done on the model alongside the results are discussed. Finally, the discussion and the computational model limitations are outlined.

### 2.1 Cell Biology

The cell is the primary structural and functional unit that makes up a living organism. Human bodies consist of eukaryotic cells which are defined as cells that include the nucleus as one of its organelles. In addition to the nucleus, eukaryotic cells are composed of a plasma membrane, cytoplasm and cytoskeleton, and many other organelles as shown in Figure 2.1 [35]. Understanding cellular biology and the mechanical properties of the cell components is critical to comprehensively manifest a realistic mechanical model of a living cell [36].

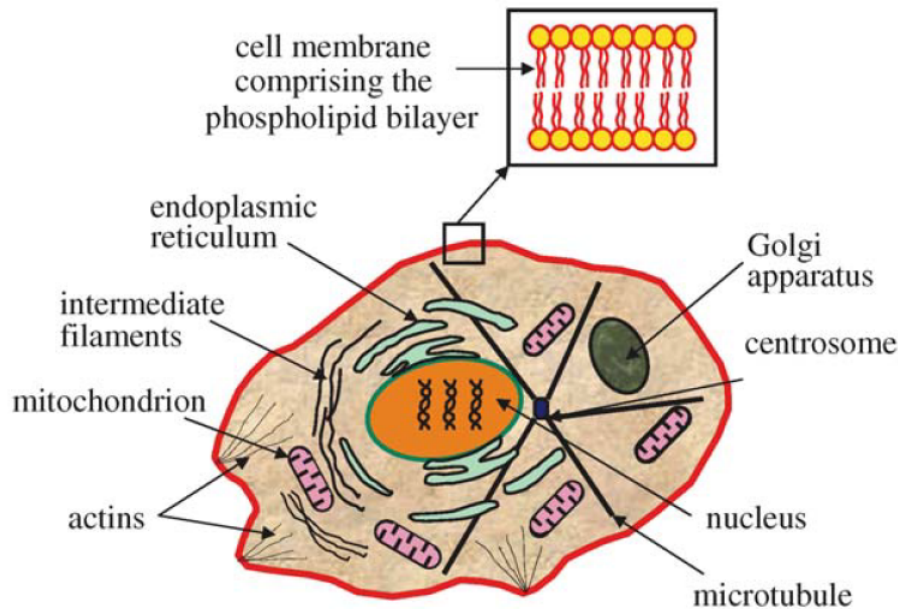


**Figure 2.1.** Eukaryotic cell [37].

### 2.1.1 Plasma Membrane

A living cell is enclosed in a semipermeable plasma membrane that separates the cell's interior from its outside environment. This elastic structure controls the movement of materials penetrating into and out of the cell [35]. The plasma membrane's thickness ranges from 3 nm to 10 nm, while the Young's moduli ranges from 0.9 MPa to 10 MPa [38, 39].

### 2.1.2 Nucleus

Eukaryotic cells contain a distinguished organelle called the nucleus. It is surrounded by a double membrane of nuclear envelope. It also accommodates DNA strands inside, which are long double helix polymer chains encoded with the genetic information of the organism [40]. Previous research articles estimated the Young's moduli of the nucleus to be between 1000 Pa to 5000 Pa [41, 42]. The ratio of nucleus size to the cell size varies for different cell types, therefore, this quantity should be adjustable depending on the model.

### 2.1.3 Cytoplasm

The cytoplasm is the semi-fluid material that submerges various organelles filling the space within the nucleus and the plasma membrane [35, 43]. The Young's moduli of the cytoplasm is found to be in the range of 100 to 500 Pa [41].

### 2.1.4 Cytoskeleton

The cytoskeleton network, found within the cytoplasm, consists of three main components: actin filaments, microtubules, and intermediate filaments [44]. The main function of these filaments is to provide the cell with structural support and play a critical role in cell movement [43]. Figure 2.2 shows the components of the cytoskeleton. Actin filaments (in red), are double-stranded twisted structures and have a diameter of 8-9 nm. They assist in cell motility and structural support. Microtubules (in green), are hollow tubular structures that originate from the microtubule-organizing center (MTOC) and have a diameter of 24-25 nm. They are important in cellular polarization. Intermediate filaments (in blue), are

rope-like structures with a diameter of 10 nm. They form a network that stretching from the nucleus to the plasma membrane providing mechanical support for the nuclear membrane [43].

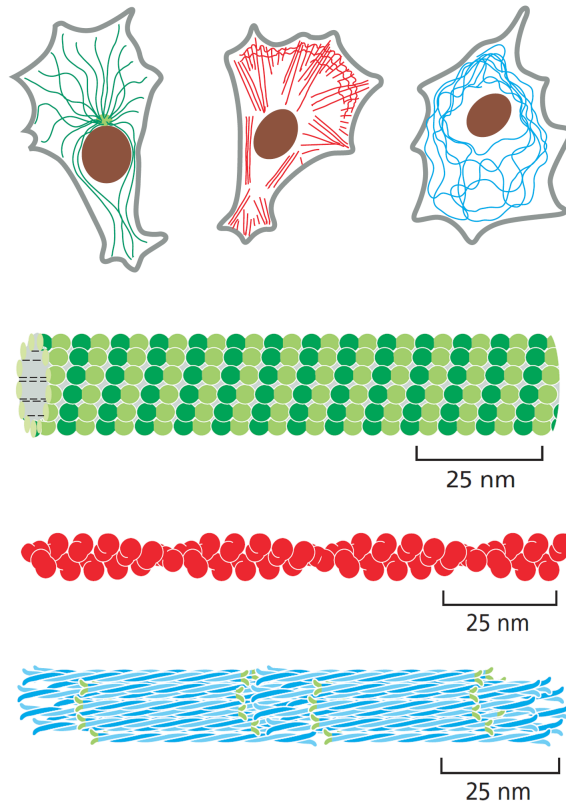


**Figure 2.2.** Cytoskeletal components and their structure: microtubules (green), actin filaments (red), and intermediate filaments (blue) [45].

## 2.2 Continuum-Tensegrity Cell Modeling

Computational modeling is a convenient tool for investigating the mechanical state of cells in response to different mechanical stimuli, as they give the ability to manifest each individual component in the cell and the cytoskeletal [46, 47]. Mechanical models along with experimental techniques can effectively explain the biomechanical behavior and reaction mechanism of cells. Cell mechanics cover the examination of cell membrane and cytoskeleton deformations, viscoelasticity, rigidity and many more mechanical properties of cells under mechanical forces [48]. Cells in our human bodies are continuously exposed

to various mechanical forces. The response of cells to these forces vary depending on the magnitude, direction and distribution of such stimuli [37].

### 2.2.1 Summary of Literature Review

Initially, researchers created cell models using the continuum approach that treated the cell as a homogeneous continuum material. Cortical shell–liquid core, power-law structural damping, and viscoelastic/elastic solid models are examples of the continuum models. Other studies have developed models using the microstructural approach, including open-cell foam models, pre-stressed cable network models, and tensegrity models. In this approach, the cytoskeleton of the cell is considered to have a critical role in the structural stability [37, 46].

In general, tensegrity interprets systems that achieve shape stability through continuous tension. The cellular tensegrity model assumes that the entire cell structure is pre-stressed where tension forces are endured by actin and intermediate filaments, whereas the microtubules withstand compression forces establishing a force equilibrium in the tensegrity structure [49]. Figure 2.3 shows a simple icosahedron model consisting of 6 struts (microtubules) and 24 cables (actin filaments). This model was used to study cell spreading by pinning the different nodes to a rigid substrate, which indicates that such attachment induces an increase in both the stiffness, and prestress in the cable elements [50].

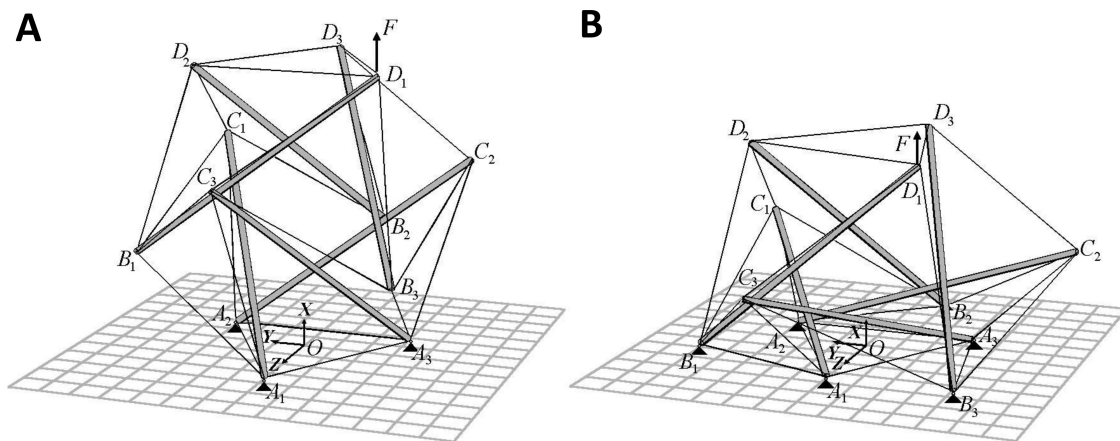


**Figure 2.3.** Tensegrity model consisting of 6 struts and 24 cables. (A) Round. (B) Spread configurations. [50]

To account for the contribution of intermediate filaments, the six-strut tensegrity model was improved as shown in Figure 2.4 to include radial cables that represent intermediate filaments bearing tension forces [51].

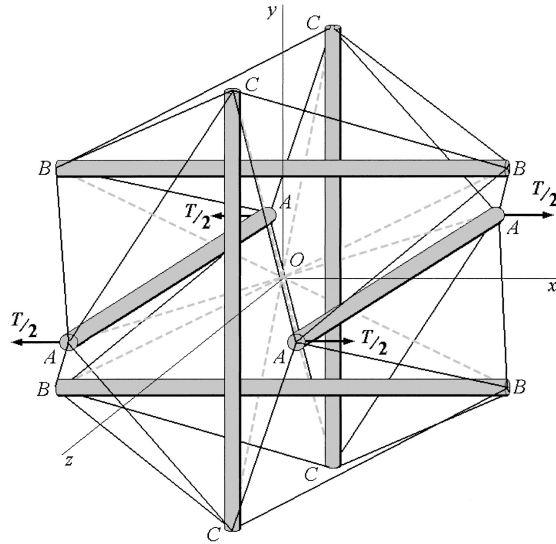


**Figure 2.4.** Tensegrity model consisting of 6 microtubule struts (AA, BB and CC), 24 actin filament cables (AB, AC and BC) and 12 intermediate filament radial cables (OA, OB and OC) [51].

Computational mechanical models created using the continuum approach have proved to be successful in estimating the overall deformation of cells. Nevertheless, this approach lacks to predict deformation on the molecular level and the inner interactions of the cell [37]. Therefore, to provide a better understanding of the cell's mechanical behavior, studies designed finite element models that combined both the continuum and the tensegrity approaches [46, 47, 52]. The hybrid solution which incorporates the continuum and the micro/nanostructural approaches will aid in recognizing the fundamental relations for the whole cell as well as for cellular components. It is therefore expected that this approach might be useful for studying cellular mechanotransduction by learning how mechanical forces exerted on the cellular microscale translate into the subcellular and cytoskeletal components at the nanoscale [37].

McGarry and Prendergast built a hybrid finite element model as shown in Figure 2.5. The continuum structure includes the nucleus and the cytoplasm, was modeled using linear isotropic elastic materials. In addition, the tensegrity structure represents the internal cytoskeleton composed of six microtubules as struts that resist compression and twenty-four actin filaments as cables withstanding tension. They investigated different models by varying the spread configurations of a rounded cell adherent to a substrate. Their findings confirmed the critical role of the cytoskeleton in establishing structural stability. Furthermore, the cytoplasm was found to be the main component after the cytoskeleton to resist deformation despite being considerably less elastic than the plasma membrane and the nucleus [46].

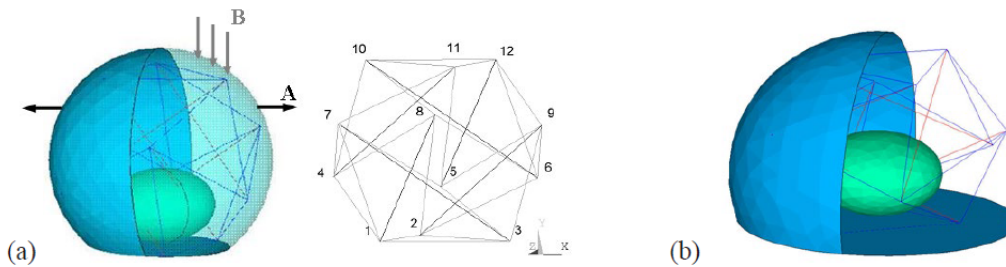


**Figure 2.5.** Finite element models (a) to (b) of adherent cells at increasingly spread configurations consisting of nucleus, plasma membrane, cytoplasm and cytoskeleton tensegrity structure of microtubules (dark/red lines) and actin filaments (light/blue lines) [46].

Bansod et al. also employed the hybrid approach in their model. Figure 2.6 demonstrates their spherical suspended continuum model consists of cell membrane, cytoplasm, and a nucleus. Furthermore, the tensegrity model includes tension bearing cables representing actin filaments, compression bearing beam elements of microtubules emerging from the MTOC and extending to the focal adhesions to form a star-like shape, and intermediate filaments connecting the nucleus to the focal adhesions. The actin filaments form a condensed network underneath the cell membrane that is important to maintain the shape of the cell. In their paper, they examined the cell model by performing the tensile and the indentation tests. The former illustrates the critical role that microtubules and actin filaments play in increasing the cell global stiffness with stretching, whereas the latter showed that the cell behavior is

regulated by the indentation site [47].

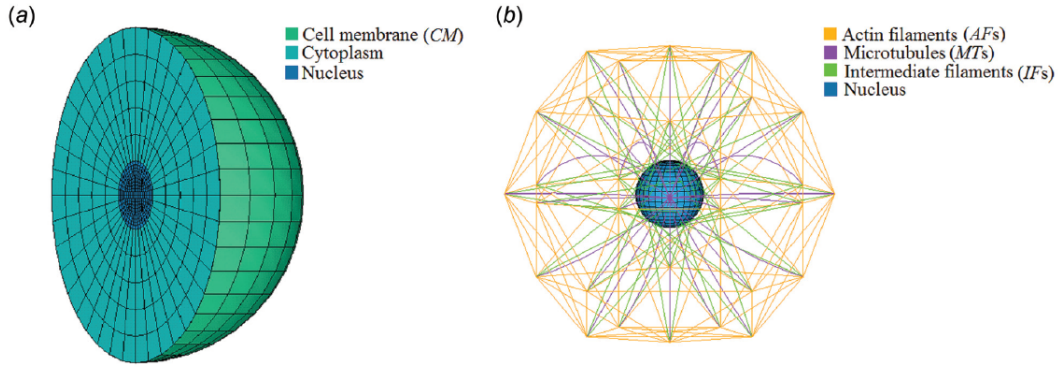


**Figure 2.6.** Finite element model of suspended cell: (a) Continuum section. (b) Tensegrity section [47].

Barreto et al. established a three-dimensional finite element cell model, using the hybrid approach, composed of cytoplasm, nucleus, actin bundles, actin cortex, and microtubules coming out of the MTOC node as shown in Figure 2.7. In their study, they performed the indentation test using a bead placed on the top of the model. Their model was utilized to estimate cell deformation under compression and shearing and to conclude the roles the cytoskeleton components play in cellular behavior. Their findings demonstrate that the key components to resist compression are microtubules and actin cortex. Also, the main components that resist shear are actin bundles and microtubules [52, 53].

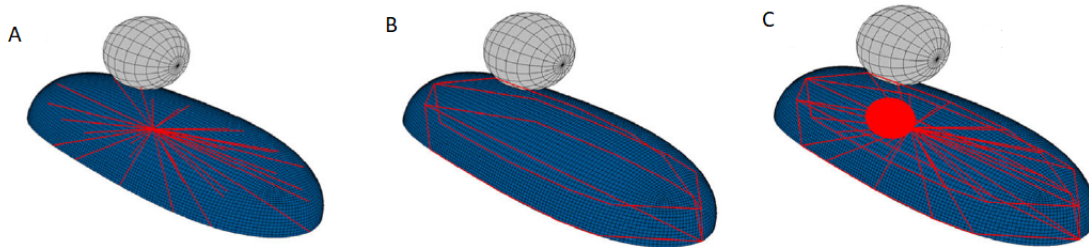


**Figure 2.7.** Finite element model of a single cell. (A) Microtubules. (B) Actin bundles. (C) Actin bundles and microtubules with respect to the nucleus [52].

A model designed by a previous lab member is shown in Figure 2.8. The cell was modeled as a dome-shaped structure that includes a plasma membrane, cytoplasm, nucleus, and microtubules originating from a microtubule-organization center (MTOC) connected to the surface of the nucleus. This model focused more on the MTOC orientation in relation to the nucleus, which is related to the experimental work done in this thesis.

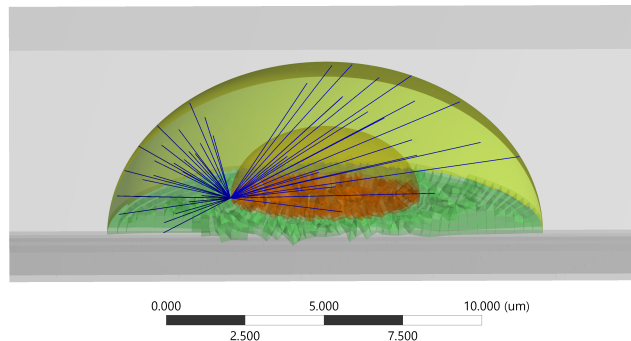


**Figure 2.8.** A three-dimensional cell model in a sliced view to allow the visualization of the internal components: microtubules (blue), cytoplasm (green), plasma membrane (yellow), glass substrate (gray), and nucleus (orange).

Computational models based on the finite element method, where a three-dimensional structure is represented as a finite number of elements and nodes, facilitate the deformation and Von Mises stress calculations under different loading conditions. The deformation is usually demonstrated as displacement. The Von Mises stress ( $\sigma_e$ ,  $N \cdot \mu m^{-2}$ ), also referred to as the effective stress, combines the stress values in each direction and can be calculated as shown in Equation 2.1 [54]:

$$\sigma_e = \left[ \frac{1}{2} \left[ (\sigma_{xx} - \sigma_{yy})^2 + (\sigma_{xx} - \sigma_{zz})^2 + (\sigma_{yy} - \sigma_{zz})^2 + 6 (\sigma_{xx}^2 + \sigma_{yy}^2 + \sigma_{zz}^2) \right] \right]^{\frac{1}{2}} \quad (2.1)$$

### 2.2.2 Continuum Model

The mechanical properties of the cell are mostly accounted for by the cytoplasm, nucleus, plasma membrane, cytoskeleton microtubules, and actin filaments. Therefore, in this study, a hybrid model was designed combining the continuum structure with the tensegrity structure. The geometry was created in Ansys Workbench v. 19.0 "DesignModeler". The continuum

structure includes plasma membrane, cytoplasm, and nucleus. Table 2.1 demonstrates the material properties used based on previous studies.

**Table 2.1.** Mechanical properties used for the continuum part of the finite element model.

Cell Component	Young's Modulus (Pa)	Poisson Ratio	Dimensions(nm)	Finite Element
Nucleus	2500	0.37	Height: 1000 Diameter: 5600	SOLID187
Cytoplasm	250	0.41	Height: 3300 Diameter: 14000	SOLID187
Plasma Membrane	$5.45 \times 10^6$	0.45	Thickness: 9	SHELL281

The objective was to create a more realistic shape of a cell, therefore instead of modeling it as a dome-shaped cell, a non-regular realistic cell shape was mimicked. An image of endothelial cells was taken through the microscope as shown in Figure 2.9. It was traced to create the base of the cytoplasm, then three curves were utilized to form the top of the model using the skin feature. Moreover, the plasma membrane was designed as a layer that circumscribe the cytoplasm by employing the surface from faces feature, and it was assigned a thickness of 9 nm. And finally, an ellipsoid was created to represent the nucleus as shown in Figure 2.10. Both the cytoplasm and the nucleus were modeled with SOLID187, which is a ten-node tetrahedral element. Whereas the plasma membrane was modeled as SHELL281, which is an eight-node shell element [55].

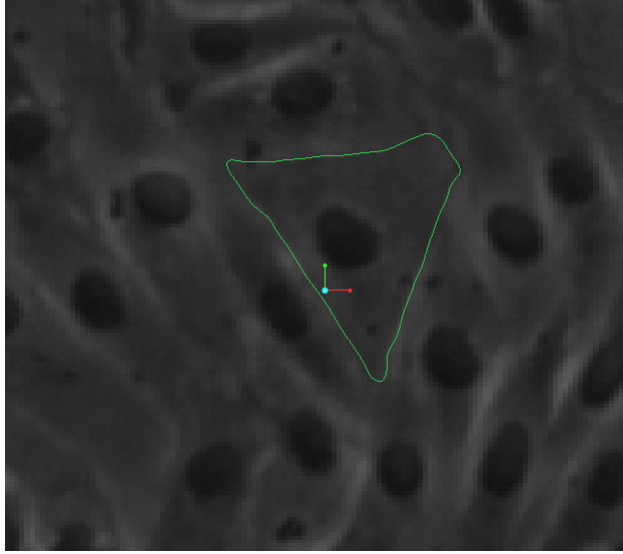


**Figure 2.9.** Microscopic image of endothelial cells.

### 2.2.3 Tensegrity Model

The second part of the hybrid model is the tensegrity structure representing the cytoskeleton that includes microtubules and actin filaments. Table 2.2 shows their assigned mechanical properties based on estimated values from previous studies.

The designed tensegrity structure consists of six microtubules connected to twenty-four actin filaments and extended to fill the interior of the cell model forming a similar shape as shown in Figure 2.10. Additionally, microtubules and actin filaments were designed as one-dimensional line bodies with a circular cross-sections. LINK180 elements were employed to model the cytoskeleton, with the compression-only (gap) option for microtubules, and the tension-only (cable) option for actin filaments [55]. This was established by inserting a code command for each line body. The corresponding cross-sectional areas assigned for microtubules and actin filaments were  $12750 \text{ nm}^2$  and  $20000 \text{ nm}^2$  respectively [36].

**Table 2.2.** Mechanical properties used for the tensegrity part of the finite element model.

Cell Component	Young's Modulus (Pa)	Poisson Ratio	Dimensions	Finite Element
Microtubule	$6.5 \times 10^{14}$	0.3	Cross-sectional area: $12750 \text{ nm}^2$ Diameter: 25 nm	LINK180 Compression-only
Actin Filament	$1.735 \times 10^9$	0.3	Cross-sectional area: $20000 \text{ nm}^2$ Diameter: 8 nm	LINK180 Tension-only

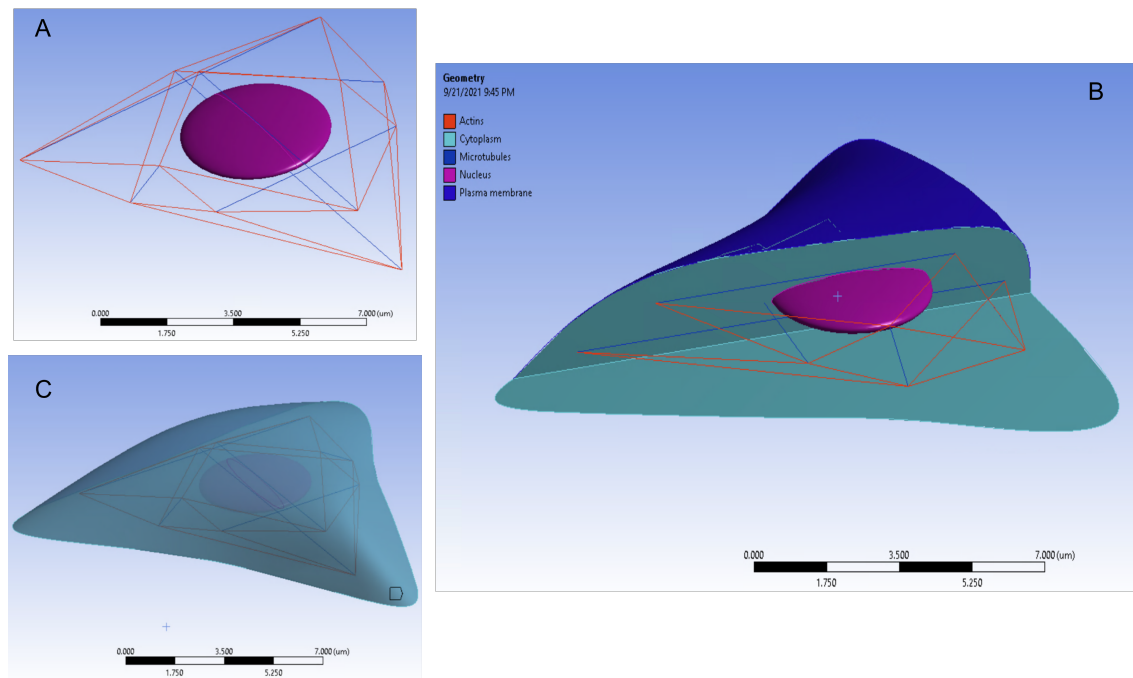


**Figure 2.10.** (A) Tensegrity part of the hybrid model includes 6 microtubules (blue) and 24 actin filaments (red). (B) A sliced view of the hybrid model to show the internal components: microtubules (blue), actin filaments (red), nucleus (purple), cytoplasm (green), and plasma membrane (dark blue). (C) A full view of the cell model with the tensegrity part inside.

## 2.3 Fluid Modeling

To model the fluid domain, Ansys Workbench v. 19.0 "Fluid Flow (Fluent)" was used. First, a rectangular channel with the dimensions  $120 \times 40 \times 90 \mu\text{m}$  as shown in Figure 2.11A was created. The inlet, outlet, wall, and wall-deform were defined, where the wall represents the remaining 4 faces and the wall-deform is at the bottom of the channel in the place of the cell model body. This channel was meshed as shown in Figure 2.11B.

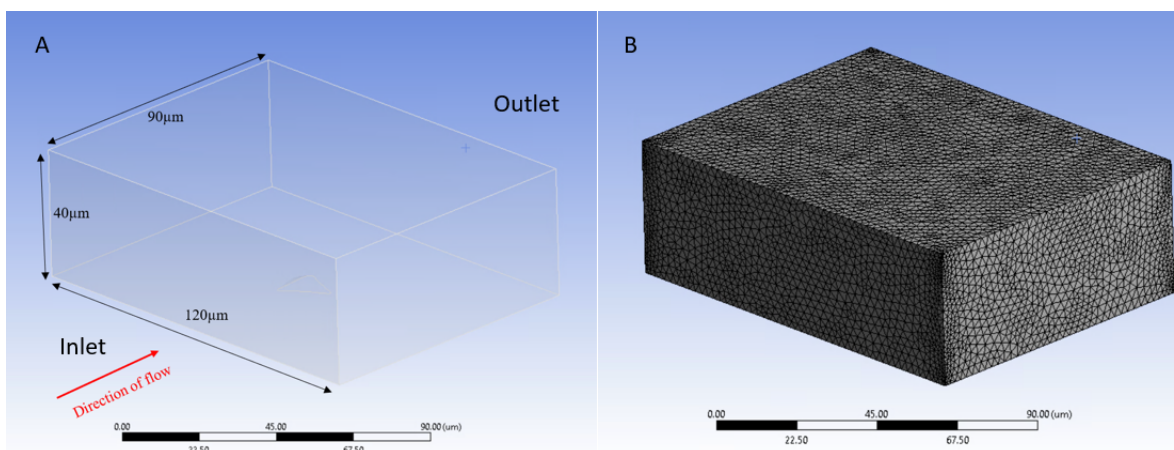


**Figure 2.11.** (A) Dimensions of the flow channel. (B) Meshing of the flow channel.

The fluid domain was assumed to have a laminar, incompressible flow of a Newtonian fluid that closely resembles water. The fluid properties assigned for the media used were a density of  $1008 \text{ kg/m}^3$ , and dynamic viscosity of  $6.965 \times 10^{-4} \text{ Pa}$ . The fluid mechanics behind the analysis performed will be discussed in detail in chapter 3 of this thesis.

For *in vitro* experiments a parallel-plate flow chamber is used to apply shear stress on a monolayer of subconfluent cells. In this computational modeling approach, a single cell was modeled to be attached to a substrate (glass plate) underneath.

## 2.4 Model Analysis

The previous section discussed how the fluid domain was created in Ansys Workbench "fluent". The geometry and the fluid flow solution were transferred into a static structural module. The channel representing the fluid domain was suppressed, and the solution was

inserted as imported pressure onto the plasma membrane where the computational dynamic fluid surface was selected as the wall-deform surface defined earlier as shown in figure 2.12.

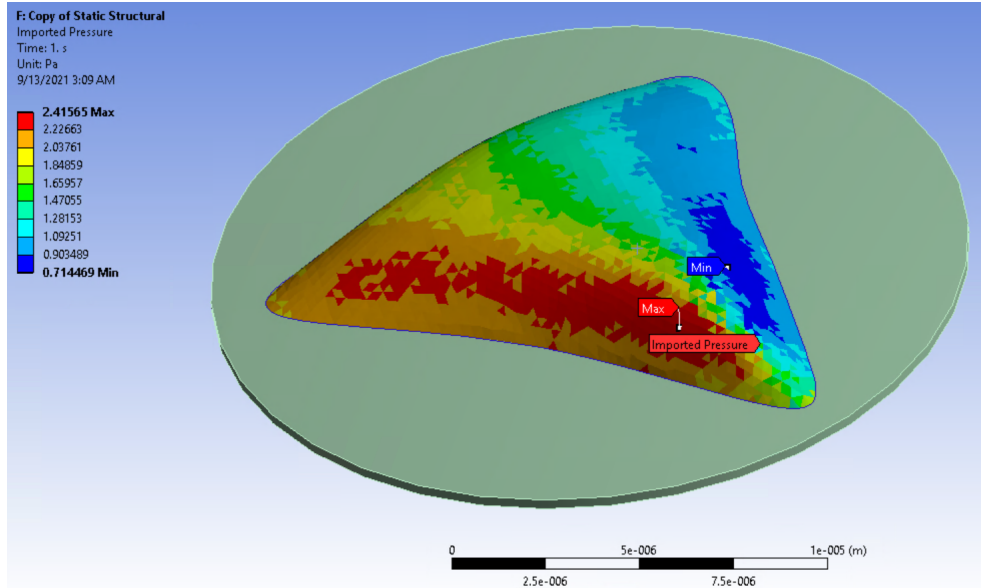


**Figure 2.12.** Pressure imported from the fluid analysis onto the plasma membrane.

The plasma membrane was meshed using a quadrilateral method with an element size of  $0.3 \mu\text{m}$ . Both the cytoplasm and nucleus were meshed with hexahedral elements of size  $0.3 \mu\text{m}$ . In addition, the line bodies of microtubules and actin filaments were meshed into 2 divisions each. The meshing of the cell model is illustrated in Figure 2.13

Bonded contacts were formed between the cytoplasm, nucleus, and plasma membrane. In addition, every microtubule line body was bonded to 8 actin filaments. 12 nodes were merged at the corners of the tensegrity model with the top and bottom faces of the cytoplasm based on their proximity. A glass plate was created under the cell model to be a fixed support for the model to provide a stable system for the software to run. Also, the bottom face of the model was attached to the glass plate.

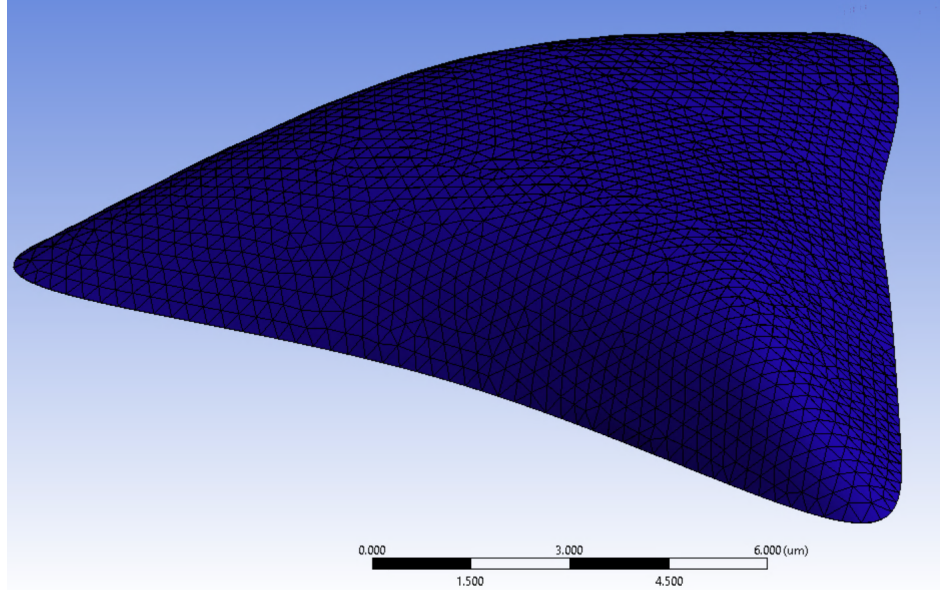


**Figure 2.13.** Meshing of the cell model.

## 2.5 Results

Running the analysis settings in section 2.4 provided various warnings and errors. The most common error message is shown in Figure 2.14. The same message appeared in some cases on the plasma membrane body. Using a smaller mesh element size for both the cytoplasm and the plasma membrane failed to get rid of this error. In addition, reducing the force applied on the model still gave the same error.

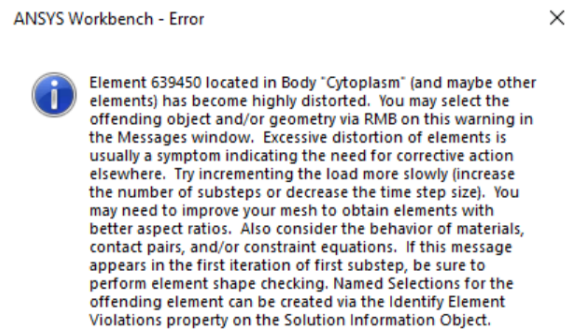


**Figure 2.14.** High distortion error message in Ansys Workbench.

Another common error was that the internal solution magnitude limit was exceeded as shown in Figure 2.15. The troubleshooting for such an error suggested that the environment must be checked for inappropriate load values or insufficient supports. It also suggested to consider adjusting the setting options of weak spring stiffness and turning on the inertia relief. The option for inertia relief failed to get rid of the error due to the non-linear properties of the model. On the other hand, adjusting the weak spring stiffness managed to avoid this error in some cases; however, the weak spring stiffness option did not prove to be a consistent solution to the error and was therefore not included in the final model.

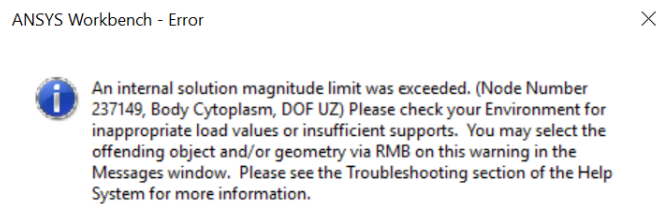


**Figure 2.15.** Internal solution magnitude error message in Ansys Workbench.

To break down the problems faced, a simple geometry was created consisting of only a cytoplasm, two microtubules, and two actin filaments. Four node merges were created at each corner of the tensegrity part and were attached to the top surface of the cytoplasm. Similar fluid and model analysis settings were used to run the solution. The total deformation of this simple geometry is shown in Figure 2.16. The simple tensegrity structure here appears to be touching the top face of the cytoplasm due to the node merges feature. However, running the analysis without these node merges failed to provide a solution.

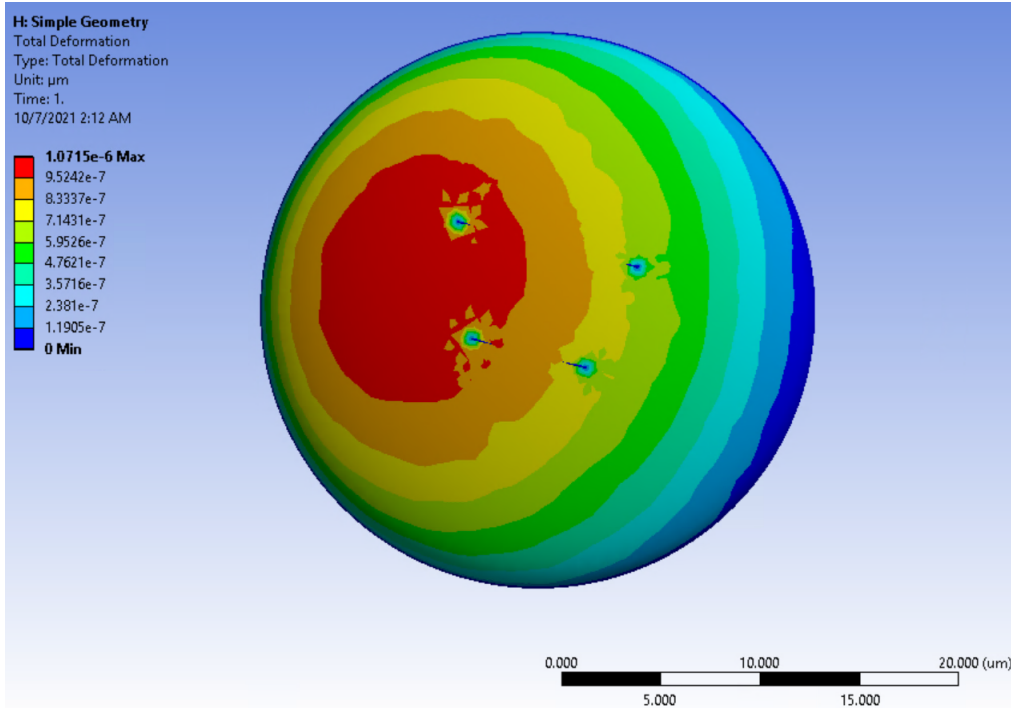


**Figure 2.16.** Total Deformation of the simple geometry model created.

## 2.6 Discussion and Limitations

The computational cell model created in this thesis had an irregular shape that resembles a more realistic cell compared to the dome or spherical-shaped models designed previously. It was assumed that the issues faced during running the analysis were because of this shape.

Although running the analysis using the simple geometry provided preliminary results that narrowed down the issues faced, the more complex model still failed to generate a valid solution. When running the simple geometry analysis, it was noticed that when the node merges created with the top surface of the cytoplasm were suppressed the solution fails. Therefore, it was believed that the issue might be related to the node merges between the tensegrity structure and the cytoplasm. In addition, the node merge feature in Ansys Workbench was only possible to merge vertices into surfaces instead of bodies. Thus, the tensegrity corners were merged to the top and bottom faces of the cytoplasm, however, the microtubules and actin filaments of the computational model created do not extend to the cytoplasm surfaces. Therefore, we assume that could be one of the reasons behind the errors.

At the beginning of this study, there were two attempts made prior to using Ansys Workbench v. 19.0 "DesignModeler". The first attempt utilized NX Siemens as shown in Figure 2.17, where there were some limitations with this software especially with the  $nm$  -  $\mu m$  scale needed for the model. Whereas, for the second attempt using Creo as seen in Figure 2.18, designing the continuum part that includes plasma membrane, cytoplasm and nucleus was successful. However, it was difficult to design the microtubules and the actin filaments in the tensegrity part of the model as one-dimensional elements using this software.

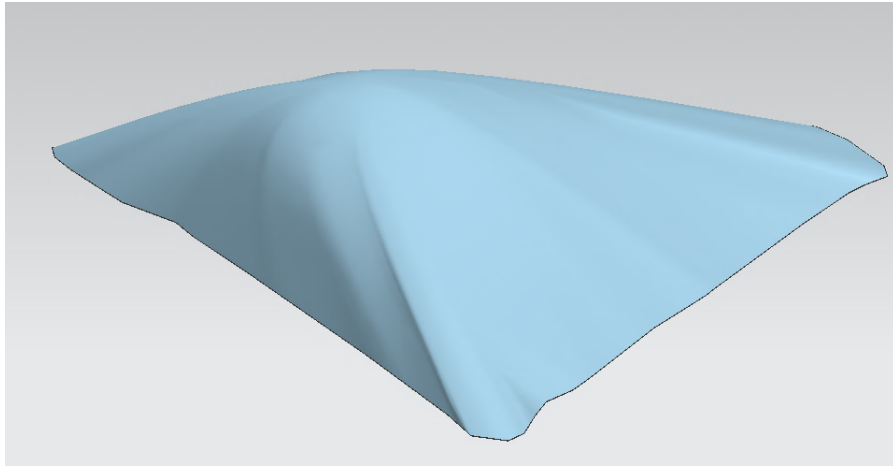


**Figure 2.17.** First attempt of a computational cell model designed in NX.

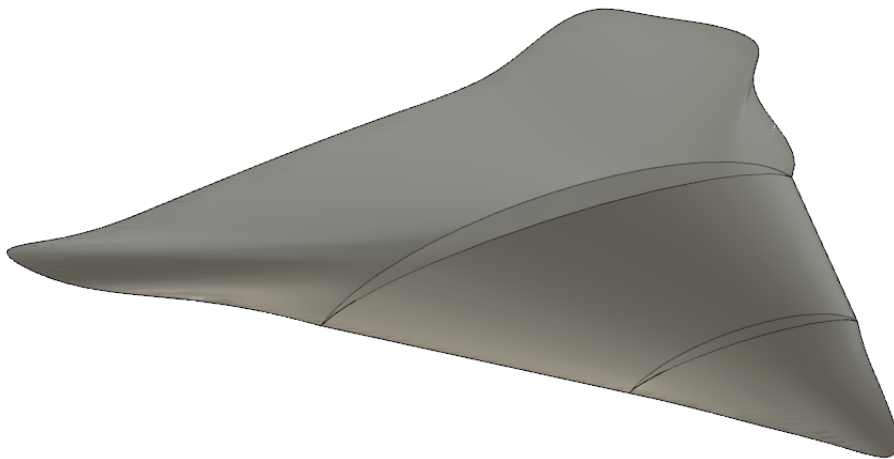


**Figure 2.18.** Second attempt of a computational cell model designed in Creo.

During this computational modeling project, the software used including creo, NX, and Ansys Workbench were accessed from IUanyware “Engineering Labs” and CNC24hours remote desktop which caused many problems such as connection issues, license keeps failing, desk memory is not enough.

### 3. EXPERIMENTAL

This chapter will demonstrate the laboratory experiments conducted in this study. It will start with the methods including cell culturing, shear stress experiment and immunostaining, then the image analysis of the nucleus and MTOC orientation will be discussed. And finally, the results and discussion will be presented.

#### 3.1 Methods

To study the effect of mechanical forces on the orientation of MTOC relative to the nucleus with wound healing, a parallel-plate flow chamber was used to exert shear stress on wild-type Lamin A and progerin-expressing bovine aorta endothelial cells. Immunofluorescence was conducted to stain and detect MTOCs. A custom MATLAB code was utilized to recognize MTOC-nucleus pairs and classify their orientation.

##### 3.1.1 Cell Culture

Bovine aortic endothelial cells (BAECs) were grown on T75 flask (Falcon), in Dulbecco's Modified Eagle Medium (DMEM) supplemented with 10% FBS (Fetal Bovine Serum, JR Scientific), 1% of L-Glutamine (Cellgro) and 2% Penicillin streptomycin (Cellgro). Cells were incubated at 37°C with 5% CO<sub>2</sub>, while changing their media every two days. When cells reach ~ 95% confluency, 1mL of suspended cells were seeded on sterile glass slides and kept in petri dishes for 24 hours to perform the shear experiment that will be explained in the next section. Two cell lines of BAEC were used in this study, progerin-expressing cells and wild-type lamin A cells.

To generate such cell lines, first human embryonic kidney (HEK293T) cells were employed to produce the retrovirus that holds green fluorescent protein (GFP)-fused wildtype-lamin A or progerin genes. The retroviral packaging that was utilized had the packaging plasmid pUMVC (Addgene #8449), the envelope plasmid pCMV-VSV-G (Addgene #8454), and the target plasmids - pBABE-puro- GFP-wt lamin A (Addgene #17662) or pBABE-puro-GFP-progerin (Addgene #17663). After transfection, viral supernatants were added onto BAECs

with polybrene at 8  $\mu\text{g}/\text{ml}$ . Then, 48 hours later drug selection procedure started and was carried on for 10 days to achieve 95% of cells with GFP positive. Only cells at passages 1-13 and within 2 weeks after the transfection experiment were used for experiments to avoid the effect of passing. The two cell lines used in this thesis were generated by my lab colleague, Yizhi Jiang, however, I maintained my own culture to carry out the experiments.

### 3.1.2 Shear Stress Experiment

We discussed in section 1.2 that endothelial cells lining blood vessel walls are subjected to mechanical forces. The following experimental setup was used to apply shear stress on endothelial cells *in vitro*. The system shown in Figure 3.1A is made up of a parallel-plate flow chamber with a bottom part that is used to hold the slide with the seeded cells, a middle part with gaskets on each side to prevent media leakage, covered by the top part that has input and outputs to allow the flow of media. The flow chamber is kept in the housing environment shown in 3.1B during the fluid flow experiment. Inside this container, there is a peristaltic pump utilized for media circulation, a heater to maintain a temperature of 37°C, and a supply of 5% CO<sub>2</sub> to ensure standard growth conditions for cells throughout the experiment [56]. To understand more about the generated laminar flow, we need to discuss some fluid mechanics.

Navier-Stokes equation is used to represent the viscous fluid laminar flow in the parallel-plate flow chamber [57]. Equation 3.1 is a simplified 2-D equation to account for movement in the x and y-direction only:

$$\rho \left( \frac{\partial u}{\partial t} + u \frac{\partial u}{\partial x} + v \frac{\partial u}{\partial y} \right) = - \frac{\partial p}{\partial x} + \mu \left( \frac{\partial^2 u}{\partial x^2} + \frac{\partial^2 u}{\partial y^2} \right) \quad (3.1)$$

where  $\rho$  is the density of the fluid,  $u$  is the velocity of the fluid,  $\mu$  is the viscosity,  $p$  is the pressure applied.

We assume that the flow is in the x-direction and symmetric velocity at  $y = \frac{h}{2}$ , the steady-state flow is shown in Equation 3.2:

$$0 = - \frac{\partial p}{\partial x} + \mu \frac{\partial^2 u}{\partial y^2} \quad (3.2)$$

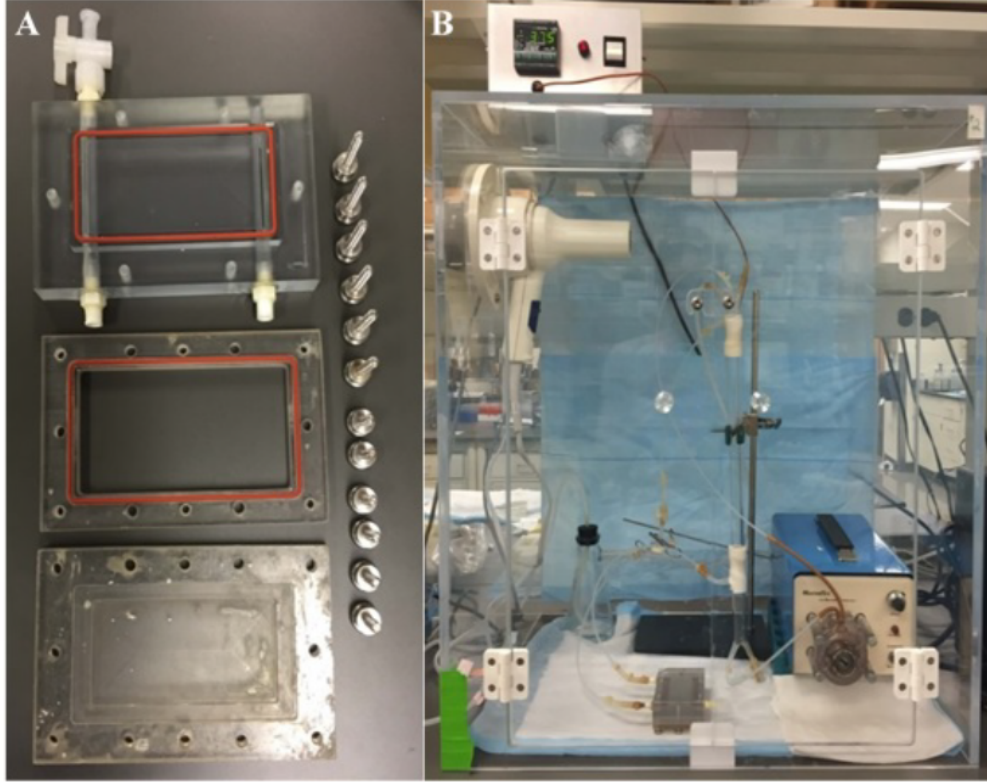


**Figure 3.1.** Setup of shear stress system: (A) Components of parallel- plate flow chamber. (B) Housing environment [56].

We integrate Equation 3.2 with the first boundary condition  $u=0$  at  $y=0$  and  $y=h$  which indicates that there is no slip at the wall-fluid interface, then integrate again with the second boundary condition  $\frac{\partial u}{\partial y} = 0$  at  $y=\frac{h}{2}$  because the maximum velocity reached is at the center of the flow, to get Equation 3.3:

$$\frac{\partial u}{\partial y} = \frac{1}{\mu} \frac{\partial p}{\partial x} \left( y - \frac{h}{2} \right) \quad (3.3)$$

Equation 3.4 shows the maximum velocity  $u_{max}$  at  $y=\frac{h}{2}$  calculated from Equation 3.3:

$$u_{max} = -\frac{1}{8\mu} \frac{\partial p}{\partial x} h^2 \quad (3.4)$$

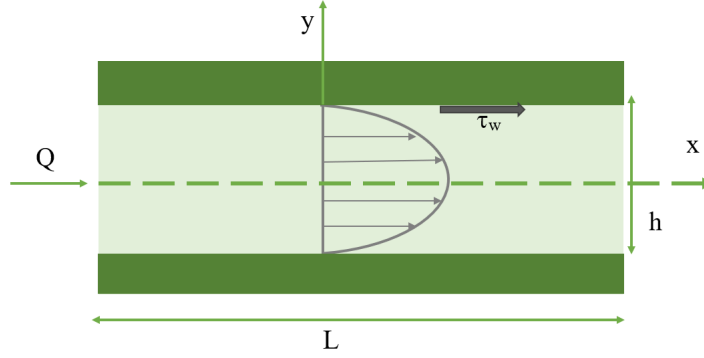


**Figure 3.2.** Fluid flow profile for the parallel-plate flow chamber.

We also know that the shear stress  $\tau = \mu \frac{\partial u}{\partial y}$ , and we substitute it into Equation 3.3 to get Equation 3.5 below:

$$\tau = \frac{\partial p}{\partial x} \left( y - \frac{h}{2} \right) \quad (3.5)$$

Equation 3.6 and Equation 3.7 shows how to calculate the volumetric flow rate  $Q$  and the average flow rate  $\bar{V}$  respectively:

$$Q = \int_A \bar{V} * d\vec{A} = -\frac{1}{12} \frac{\partial p}{\partial x} h^3 \quad (3.6)$$

$$\bar{V} = \frac{Q}{A} = \frac{1}{12} \frac{\partial p}{\partial x} h^2 = \frac{\dot{m}}{\rho A} \quad (3.7)$$

where  $\dot{m}$  is the mass flow rate. Also, it is noted from Equation 3.4 and Equation 3.7 that  $\bar{V}$  and  $u_{max}$  are lineally correlated. Further simplifications by substituting 3.7 into 3.4 gives Equation 3.8 below:

$$\frac{\partial p}{\partial x} = -\frac{12\mu\dot{m}}{h^2\rho A} \quad (3.8)$$

Then, we substitute Equation 3.8 into Equation 3.5 to get:

$$\tau = -\frac{12\mu\dot{m}}{h^2\rho A} \left( y - \frac{h}{2} \right) \quad (3.9)$$

At the walls, when  $y = 0$ , the shear stress is shown in Equation 3.10:

$$\tau = -\frac{6\mu Q}{hA} \quad (3.10)$$

Thus, if we assume the height and area to be constants, the shear stress is linearly dependent on the viscosity  $\mu$  and the volumetric flow rate  $Q$ .

After discussing the setup and the fluid mechanics behind the flow system used in this study, we will clarify the experiments performed.

In section 3.1.1, it was mentioned that cells were seeded on glass slides 24 hours before shearing. The cells were scraped with a pipet tip in a horizontal and vertical straight lines to create a “scratch”. One slide was exposed to 15 *dyn/cm*<sup>2</sup> shear stress for 4 hours, this represents the sheared group. Whereas, another slide remained in the incubator at 37°C with 5% CO<sub>2</sub> without external stimulus for the duration of 4 hours, this represents the static control group.

### 3.1.3 Immunofluorescence

Immunostaining was carried out to study the effect of shear stress on progerin-expressing and wild-type BAECs. After running the shear stress for 4 hours, the flow chamber was disassembled under the hood and the sheared slide was transferred into a petri dish. The static control slide was taken out of the incubator. The sheared and static control group of cells were first washed three times using Phosphate-Buffered Saline (PBS). Next, cells were fixed with 4% paraformaldehyde (PFA) for 15 minutes, to preserve cell morphology and cross-link proteins [58]. Then, cells were permeabilized with 0.2% of Triton X-100 for 15 minutes to allow the antibody to pass through the plasma membrane. Afterward, cells were washed with PBS three times for 5 minutes each and blocked using 1% Bovine Serum Albumin (BSA) for one hour, to inhibit non-specific bindings [59].

For MTOC staining, blocked cells were incubated with anti- $\gamma$ -tubulin antibody conjugated with Alexa Fluor 594 (Novus Biologicals) at 1:400 dilution in 1% BSA for 16 hours (overnight), in the dark to prevent the loss of fluorescent signal. Then, cells were washed three times with PBS for 5 minutes each. After that, cells were stained for nucleus by using

Hoechst blue stain solution at 1:1000 dilution for 15 minutes in the dark, washed with PBS three times, and stored in the dark at 4°C until ready for the next step under the microscope.

Image acquisition was obtained using a Leica DMI3000B fluorescent microscope with the 40X magnification objective lens.

### **3.1.4 Image Analysis of the Nucleus and MTOC**

There were three regions of interest in this study for each slide, the first two were near the horizontal and vertical wound edges, while the third one was a full area of cells away from any wounds to be considered as a control region.

The images were analyzed to determine the orientation of the nucleus and the MTOC using a custom MATLAB algorithm created by a previous lab member. The code runs through the images one by one where the MTOC-nucleus pairs were selected manually, and the output is given as a spreadsheet table that includes the orientation and the categorization of the MTOCs.

The MATLAB algorithm performed two methods of analysis to investigate the MTOC position in relation to the nucleus. The first method determined the MTOC orientation as a relative angle between the flow direction and a line extending from the nucleus's center to the MTOC as shown in Figure 3.3A. This angle ranges from 0 degrees which implies that the MTOC's location is downstream in relation to the flow direction and the nucleus, to 180 degrees which implies that the MTOC's location is upstream in relation to the flow direction and the nucleus. The second method classified the MTOC orientation relative to the nucleus into four categories as shown in Figure 3.3B. Class 1 represents MTOCs as downstream of the nucleus, and class 2 represents MTOCs as downstream of the nucleus's midpoint which also included class 1 MTOCs. Similarly, class 3 had cells with MTOCs as upstream of the nucleus's midpoint, and included class 4 of cells with MTOCs upstream of the nucleus [60].

When the images were first inserted into the MATLAB code, they were converted to grayscale to recognize nuclei. A Gaussian filter was utilized to smooth the images, then they were transformed into black and white binary images. To avoid any debris in the images, borders and small structures below a certain threshold were suppressed. In addition, a

MATLAB for-loop was used to ensure running through all the images in the folder and picking the MTOC-nucleus pairs in each. MATLAB region-props functions were employed to find the cell properties such as the coordinates of the nucleus centroid. To calculate the MTOC angle, first, the distance between the MTOC picked and the nucleus was calculated using the Pythagorean theorem, then an inverse trigonometry function was used. Afterward, the before-mention angle was compared to the nucleus midpoint then the classes of the MTOC were determined via MATLAB if-statements.

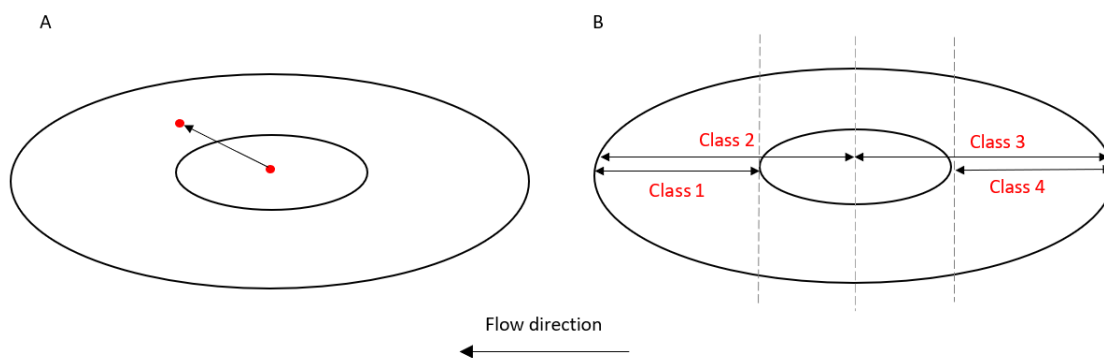


**Figure 3.3.** (A) MTOC-nuclear orientation as an angle ranging from 0 to 180 degrees. 0 means that MTOC was located downstream of the shear direction and the nucleus, while 180 means that MTOC was located upstream of the shear direction and the nucleus. (B) Categorized distribution of MTOC-nuclear orientation. MTOCs were grouped as downstream of the nucleus (scored 1), downstream of the midpoint of the nucleus (scored 2), and upstream of the midpoint of the nucleus (scored 3), and cells upstream of the nucleus (scored 4).

### 3.1.5 Statistical Analysis

Microsoft Excel was used to plot the graphs in this study. The MATLAB output provides the average and the standard error of the mean (SEM) of MTOC Orientation angle. Thus, data for MTOC-nuclear orientation angle were represented as mean  $\pm$ SEM. The error bars in the plots represent  $\pm$ SEM. Student's t-test was conducted and p-values were calculated to show the statistical significance and to compare every two groups in column bar plots.

## 3.2 Results

The results of the experimental work done throughout this study to investigate the MTOC orientation of wild-type and progerin-expressing BAECs under shear stress in the presence of vertical and horizontal wounds will be presented in two different ways according to the method of measurement described earlier. The first method presents the MTOC orientation as an angle ranging from  $0^\circ$  to  $180^\circ$ . The second method presents the MTOC location by categorizing them into four groups.

### 3.2.1 MTOC-Nuclear Orientation Angle is Opposite Between Wild-Type and Progerin Cells in Vertical Wound Upstream and Downstream of Flow

As previously mentioned, the control group of cells were not subjected to any shear stress and will be referred to as static, whereas the experimental group of cells were exposed to fluid flow for 4 hours and will be referred to as sheared in the following results. The regions of interest for the static group of cells are the full area away from any wound/scratch, the horizontal and the vertical areas near the wound.

The results shown in Figure 3.4A demonstrate both the wild-type and progerin-expressing cells under static conditions. In the full region, the MTOC orientation angle for the wild-type cells was  $82.6 \pm 3.46^\circ$ , whereas for the progerin cells it was  $89.6 \pm 4.80^\circ$ . The MTOC orientation angle near the vertical wound area for the wild-type and progerin cells was  $83.8 \pm 4.47^\circ$  and  $85.1 \pm 4.25^\circ$  respectively. In addition, the results near the horizontal wound area for the wild-type cells were  $86.5 \pm 3.20^\circ$  and  $96.2 \pm 3.75^\circ$  for the progerin cells (\* P = 0.05 compared to wild-type cells).

The results shown in Figure 3.4B illustrates both the wild-type and progerin-expressing cells after exposure to 4 hours of shear stress conditions. In the full region, the MTOC orientation angle for the wild-type cells was  $79.2 \pm 3.62^\circ$ , whereas for the progerin cells it was  $82.0 \pm 3.28^\circ$ . As for the vertical scratch, there were two regions of interest to indicate the upstream and downstream of the fluid flow. For the vertical upstream of the flow, the MTOC orientation angle for the wild-type and progerin cells was  $89.5 \pm 5.47^\circ$  and  $83.9 \pm 4.17^\circ$  respectively. The MTOC orientation angle for the wild-type cells near the vertical

downstream of the flow wound edge was  $92.7 \pm 6.61^\circ$ , whereas for the progerin cells it was  $78.8 \pm 4.10^\circ$  (\*\* P = 0.08 compared to wild-type cells). In addition, the results near the horizontal wound area for the wild-type cells were  $78.5 \pm 4.57^\circ$  and  $88.0 \pm 2.68^\circ$  for the progerin cells (\*\* P = 0.08 compared to wild-type cells).

It is noticed that the average MTOC orientation angle for wild-type cells under static normal conditions in all regions is almost the same with a mean of  $84.3^\circ$ . On the other hand, with the progerin cells under static conditions, the results seem to vary.

It is observed that in the full region away from any vertical or horizontal wounds, the relationship between wild-type and progerin cells was similar under both static and shear conditions. However, a difference in the MTOC orientation between wild-type and progerin cells becomes visible under shear stress near vertical wounds. Comparing the wild-type cells near the vertical region, the MTOC orientation shifts slightly upstream (the angle increases) with shear compared to static. This shift is higher near the vertical downstream of flow region. On the other hand, with progerin cells near the vertical wound, under shear conditions the MTOC orientation shifts slightly downstream (the angle decreases) relative to static.

Surprisingly, it is observed that in the horizontal region in both the static and the sheared group, the progerin's MTOC orientation angle had an approximate  $10^\circ$  increase compared to that of the wild-type cells. Under static conditions, the orientation angle increased in progerin cells to be  $96.2 \pm 3.75^\circ$  compared to being  $86.5 \pm 3.20^\circ$  in wild-type cells. Moreover, under the 4 hour sheared conditions, the orientation angle increased in progerin cells to be  $78.5 \pm 4.57^\circ$  compared to being  $88.0 \pm 2.68^\circ$  in wild-type cells.

Figure 3.5 shows representative images for wild-type and progerin-expressing BAECs under static and after 4 hours of shear stress conditions. Three regions of interest were shown for every group to include the full region away from wounds, the vertical and the horizontal wound areas.

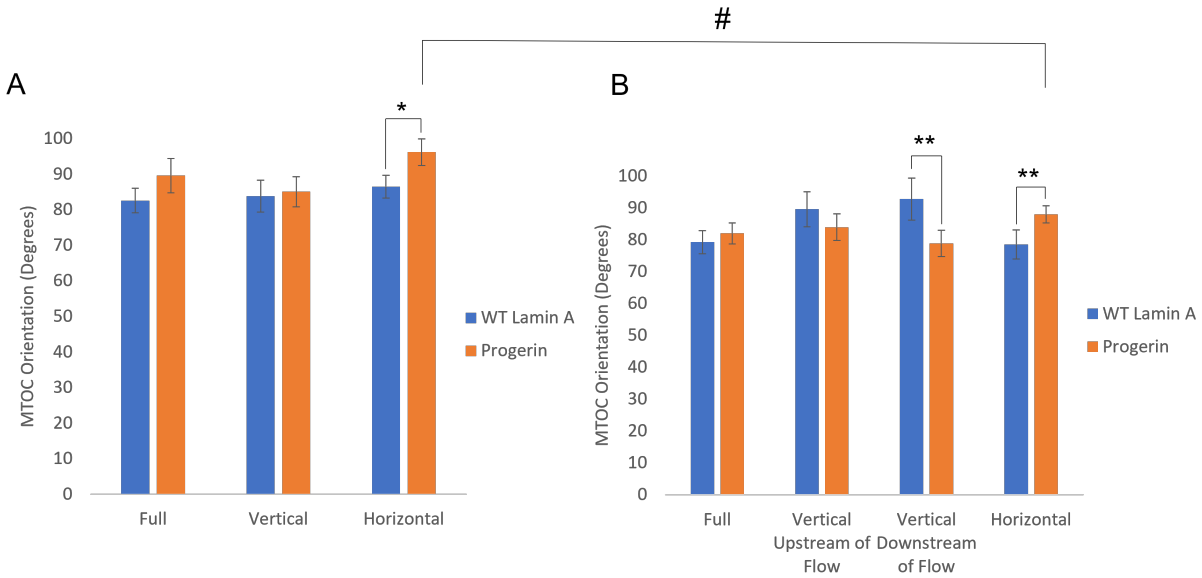


**Figure 3.4.** The average of MTOC-nuclear orientation angle (ranges from 0 to 180 degrees) in wild-type and progerin-expressing BAECs under static and sheared conditions. 0° means that MTOC was located downstream of the shear direction as to the nucleus, while 180° means that MTOC was located upstream of the shear direction as to the nucleus. The full region represents the area away from wounds, the vertical region is the area near the vertical wound and the horizontal region is the area near the horizontal wound. (A) Wild-type and progerin-expressing cells under static conditions. (\* P = 0.05, wild-type vs. progerin cells) (B) Wild-type and progerin-expressing cells after 4 hours of shear stress. (# P = 0.07 static vs. sheared progerin cells , \* \* P = 0.08, wild-type vs. progerin cells).

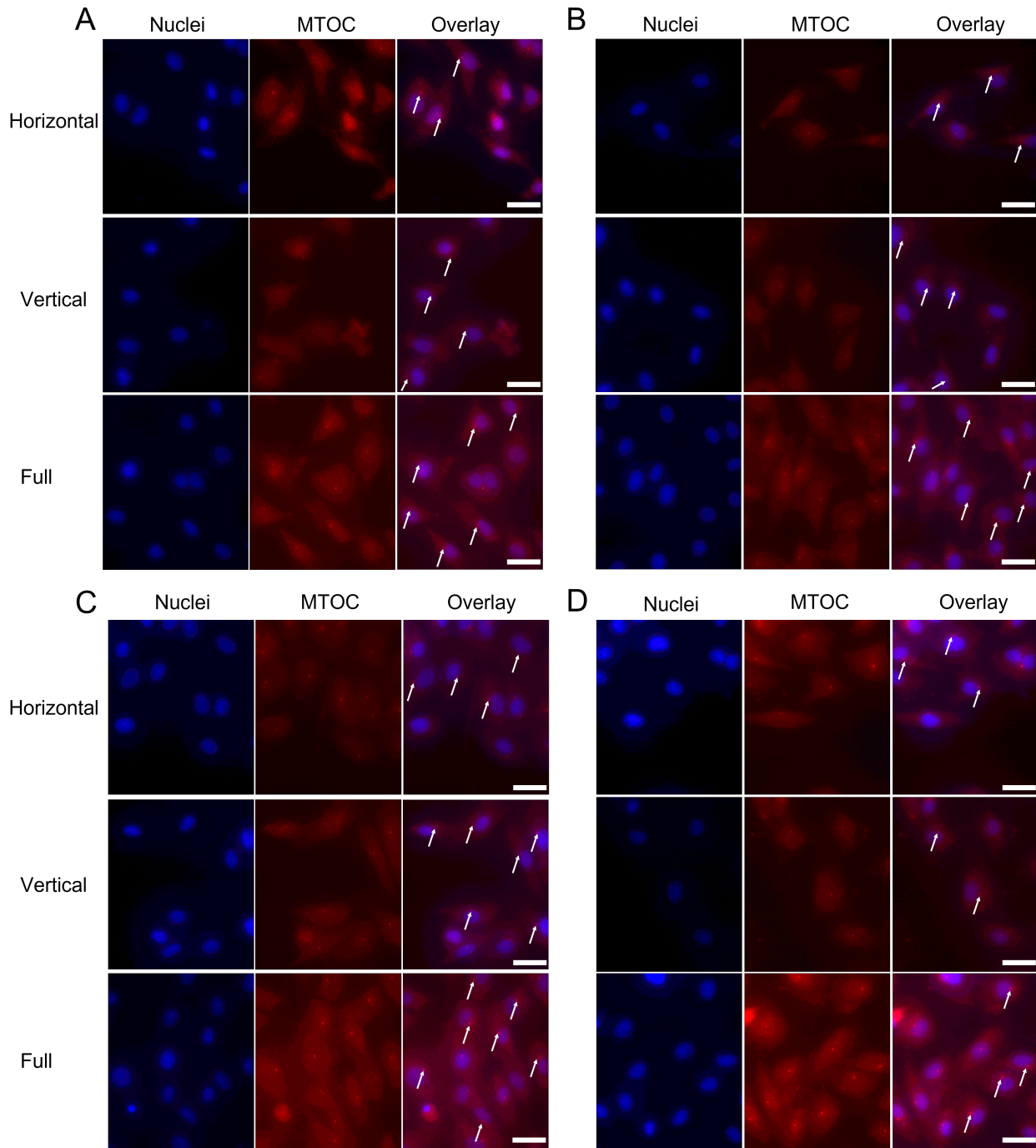


**Figure 3.5.** Representative images of wild-type and progerin-expressing BAECs labeled for nuclei and MTOC under static and sheared conditions. (A) Wild-type cells under static conditions. (B) Progerin-expressing cells under static conditions. (C) Wild-type cells after 4 hours of shear stress. (D) Progerin-expressing cells after 4 hours of shear stress. Cells from left to right were shown: stained for nuclei with Hoechst, stained for MTOC with anti- $\gamma$ -tubulin conjugated with Alexa Fluor 594, and overlay of both stains. Scale bar - 25  $\mu\text{m}$

### 3.2.2 Classified Positioning of MTOC Show Different Response to Flow at The Vertical Wound Edge Between Wild-Type and Progerin Cells

As previously mentioned, the analysis done with MATLAB code provides an output of four classes of the MTOC-nucleus orientation as shown in Figure 3.3B. Class 1 represents MTOCs as downstream of the nucleus, and class 2 represents MTOCs as downstream of the nucleus's midpoint which also included class 1 MTOCs. Similarly, class 3 had cells with MTOCs as upstream of the nucleus's midpoint and included class 4 of cells upstream of the nucleus [60].

For plotting purposes, these categories were changed into: (A) Two groups: downstream = class 2 that also includes class 1 and upstream = class 3 that also includes class 4. (B) Four groups: group A = class 1, group B = class 2 - class 1, group C = class 3 - class 4 and group D = class 4. Figure 3.6 represents plots of wild-type and progerin-expressing cells under static and sheared conditions according to the upstream and downstream groups. Additionally, Figure 3.7 demonstrate similar results by plotting them into four groups.

Results in Figure 3.6A and 3.7A show MTOC-nuclear orientation as percentages of wild-type cells under static conditions without exposure to shear stress. These graphs demonstrate that with wild-type cells under normal conditions the distribution of MTOC-nuclear orientation is nearly similar in all the regions. In the full region away from any wound areas, it is observed that 55.8% of the MTOC-nuclear pairs picked had their MTOCs in the downstream group relative to the nucleus, divided into 44.2% in group B and 11.6% in group A. Also, near the vertical wound, 53.3% of the pairs are in the downstream of the nucleus with 35.5% in group B and 17.8% in group A. Near the horizontal wound, the distribution is almost the same in both groups with 49.8% in the downstream and 50.2% in the upstream.

Results in Figure 3.6B and 3.7B show MTOC-nuclear orientation of progerin-expressing cells under static conditions. Here, it is noticed that in the full region there was no preference for either group as the percentages were 50.9% and 49.1% for the downstream and upstream groups respectively. On the other hand, MTOCs of cells near the vertical wound had a slight preference to be in the downstream group with a percentage of 54.8%. The opposite is true near the horizontal wound, as 55.7% of the pairs were in the upstream group.

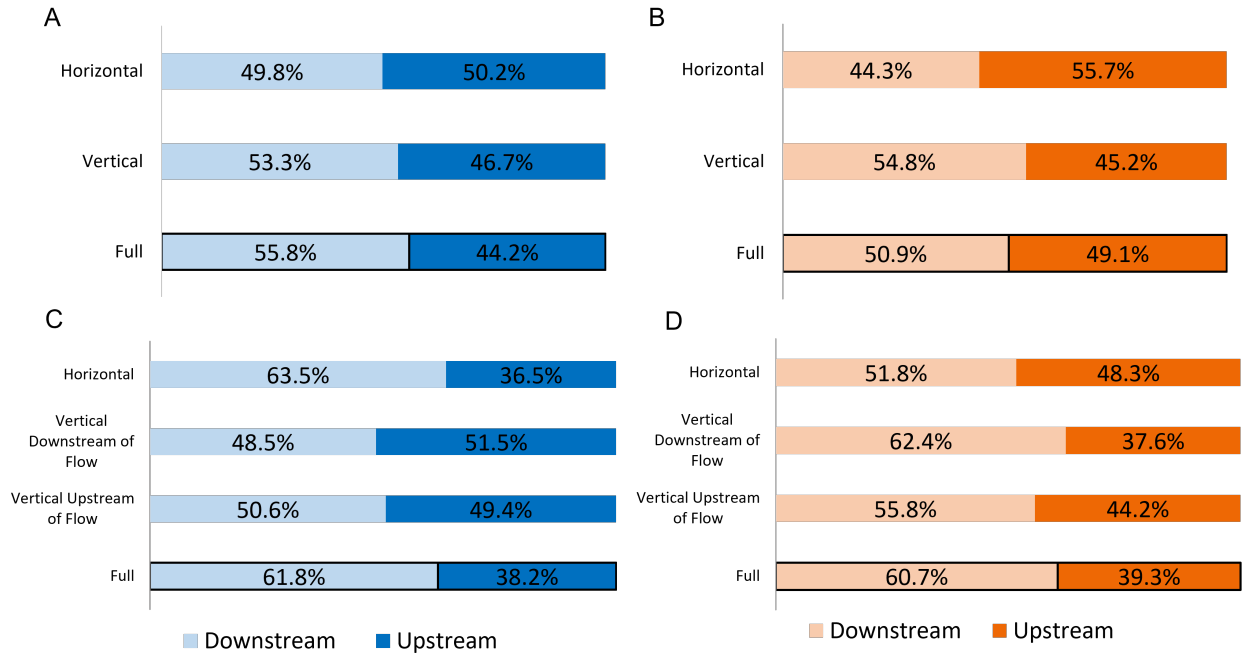


**Figure 3.6.** Categorized distribution of MTOC-nuclear orientation in wild-type and progerin-expressing BAECs in static and sheared conditions. The downstream here is class 2 including class 1. While the upstream is class 3 including class 4. The full region represents the area away from wounds, the vertical region is the area near the vertical wound and the horizontal region is the area near the horizontal wound. (A) Wild-type cells under static conditions. (B) Progerin-expressing cells under static conditions. (C) Wild-type cells after 4 hours of shear stress. (D) Progerin-expressing cells after 4 hours of shear stress.

Results in Figure 3.6C and 3.7C show MTOC-nuclear orientation of wild-type cells after 4 hours of shear stress. It is noted that cells away from scratch are leaning towards the downstream group with a percentage of 61.8% of the MTOC-nuclear pairs. However, no detectable bias was shown near the vertical wound. In the vertical upstream of the flow, the percentages for the upstream and downstream groups were 50.6% and 49.4% respectively. For the vertical downstream of the flow region, the percentages were 48.5% and 51.5% for the upstream and downstream groups respectively. It is observed that 63.5% of the MTOC-nuclear pairs are in the downstream group near the horizontal wound.

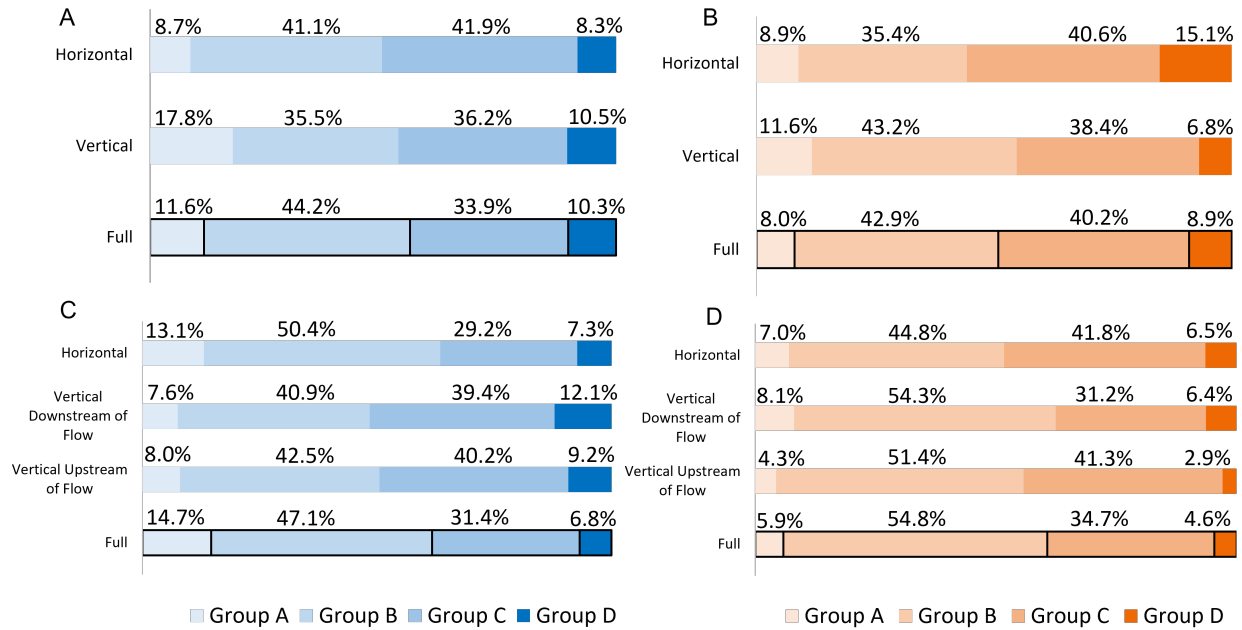


**Figure 3.7.** Categorized distribution of MTOC-nuclear orientation in wild-type and progerin-expressing BAECs in static and sheared conditions. Group A is downstream of the nucleus, group B is downstream of the midpoint of the nucleus, group C is upstream of the midpoint of the nucleus, and Group D is upstream of the nucleus. The full region represents the area away from wounds, the vertical region is the area near the vertical wound and the horizontal region is the area near the horizontal wound. (A) Wild-type cells under static conditions. (B) Progerin-expressing cells under static conditions. (C) Wild-type cells after 4 hours of shear stress. (D) Progerin-expressing cells after 4 hours of shear stress.

Results in Figure 3.6D and 3.7D show MTOC-nuclear orientation of progerin-expressing cells after 4 hours of shear stress. In the full region, the preference was obvious towards the downstream group with a percentage of 60.7% of the pairs. For the vertical upstream of the flow, the percentages for the upstream and downstream groups were 55.8% and 44.2% respectively. For the vertical downstream of the flow region, the percentages were 62.4% and 37.6% for the upstream and downstream groups respectively. In addition, no bias for either group was visible near the horizontal wound with 51.8% in the downstream and 48.3% in the upstream group.

### 3.3 Discussion

Previous studies that involve *in vitro* experiments illustrate that flow induces MTOC polarization upstream of the nucleus [24, 25], or MTOC polarization downstream of the nucleus [60–62]. In our wild-type and progerin-expressing BAECs, steady shear stress of 15  $dyn/cm^2$  applied for 4 hours consistently orients MTOC downstream relative to the nucleus (see Figure 3.4B and 3.6C and D).

Our data suggest that progerin-expressing cells are affected by flow more significantly than wild-type cells (see Figure 3.4). We believe that progerin makes the cell more susceptible to shear stress, therefore progerin-expressing cells become more easily guided by flow in the presence of wound healing than wild-type cells.

Furthermore, our findings demonstrate that the biggest distinction between wild-type and progerin-expressing BAECs was seen around the vertical wound edges under shear stress upstream and downstream of the flow (see Figure 3.4B). At the wound edge upstream of the flow, the angle of the MTOC orientation for the wild-type cells is slightly leaning towards the upstream, whereas it was leaning toward the downstream for progerin cells. Similar results were observed at the wound edge downstream of the flow with a p-value = 0.08 for wild-type vs. progerin cells. In conclusion, the angle for the MTOC-nuclear orientation at the vertical wound upstream and downstream of flow was opposite between wild-type vs. progerin-expressing BAECs.

Moreover, it was observed that the MTOC orientation angle for wild-type cells was fairly consistent under static conditions (see Figure 3.4A). In addition, the classified positioning method showed that wild-type under normal conditions had their MTOCs distributed fairly equally between the downstream and the upstream group in all the regions (see Figure 3.6A). These findings are in agreement with previous research stating that MTOCs are randomly positioned relative to the nucleus in the absence of shear stress [25, 60].

Our data indicate that shear alone was not enough to cause a noticeable change in the orientation angle of the MTOC, as it was observed the correlation between wild-type and progerin cells stayed the same under both static and shear conditions in the full area away from the wound (see Figure 3.4). On the other hand, the classified positioning method

demonstrates that shear alone away from wound edges shifted the MTOCs towards the downstream group with both wild-type and progerin-expressing cells with percentages of 61.8% and 60.7% respectively (see Figure 3.6C and D). These findings confirmed a preceding study by McCue et al. which showed that endothelial cells after exposure to 24 hours of shear stress causes most MTOCs to orient downstream of the nuclear midpoint [60], and another study by Dragt et al. that illustrates Human umbilical vein endothelial cells (HUVECs) under sustained shear stress of  $10 \text{ dyn/cm}^2$  for 5 days prompted a significant MTOC translocation towards the downstream side of the nucleus [62].

In addition, our data for the classified positioning of MTOCs at the vertical wound edges showed different responses to fluid flow between wild-type and progerin-expressing cells (see Figure 3.6C and D). For the wild-type cells, the distribution of the MTOCs is almost random between the downstream and upstream groups for both edges of the vertical wound, whereas for progerin-expressing cells more MTOCs are found in the downstream group for both vertical wound edges upstream and downstream of the flow.

Although the hypothesis was that the MTOC orientation might shift from upstream to downstream of the nucleus with wound healing under shear stress, our findings in this study couldn't confirm this. For our wild-type cells, shear stress alone away from wound areas caused the MTOCs to orient downstream of the nucleus, however, near the vertical wound edges the MTOC were distributed equally between the downstream and the upstream groups (see Figure 3.6C). On the other hand, with our progerin-expressing cells, shear stress in the full region and around both vertical wound edges caused the MTOCs to orient downstream relative to the nucleus (see Figure 3.6D).

In addition, the custom MATLAB code utilized in this study caused some limitations because it involved manual picking of the MTOC-nucleus pairs which was very time-consuming and subject to human error.

## 4. CONCLUSIONS AND SUMMARY

### 4.1 Conclusions

Endothelial cells line up blood vessels and are constantly exposed to mechanical forces. Microtubule-organizing center (MTOC), a structure from where microtubules originate, plays a role in the polarization of the cell and therefore is important in cell migration and wound healing.

In this thesis, a continuum-tensegrity model was designed. The objective of this computational model was to study the cell mechanics under shear stress. In summary, the model includes a plasma membrane, cytoplasm, and a nucleus representing the continuum part and a tensegrity structure consisting of microtubules and actin filaments. The fluid domain was created as a rectangular flow channel with the cell model placed at the bottom. Unfortunately, it was not possible to have conclusions for this analysis, the next section will discuss the future directions needed.

Moreover, *in vitro* experiments conducted in this thesis focused on analyzing the orientation of MTOC relative to the nucleus under shear stress with the presence of wound healing. It was hypothesized that when endothelial cells are exposed to fluid flow and when there is wound healing, the MTOC might relocate from upstream to downstream of the nucleus depending on the direction of the wound area.

To summarize, wild-type lamin and progerin-expressing BAECs were examined under static and after 4 hours of shear stress conditions. The orientation of the MTOC relative to the nucleus was measured in two ways using a custom MATLAB code. Our results of the MTOC-nuclear orientation angle between wild-type and progerin-expressing BAECs were opposite at the vertical edge upstream and downstream of flow.

### 4.2 Future Work

The computational tensegrity-based cell model designed in this thesis provides just the basis for further improvements to be done. First, the analysis failed to provide a solution, thus additional work is needed to investigate the reasons behind this in order to solve them.

Afterward, the computational results should be verified and validated by performing convergence and accuracy checks. In addition, a comparison between the computational and experimental results should be done.

Furthermore, the tensegrity structure built in this study consists of only 6 microtubules and 24 actin filaments. Further enhancement can be achieved by building the microtubules as line bodies emerging from one node near the nucleus to resemble the structure of the MTOC to include a more detailed cytoskeleton.

As for the experimental work of this thesis, further experiments might involve exposure to shear stress for a longer duration to confirm if similar results will be demonstrated. In addition, more data is needed to further confirm the statistical significance of this study.

Moreover, our experimental data illustrated that MTOC orients downstream relative to the nucleus, however, from literature, this was conflicted as some studies show the location as upstream while others found out that MTOC orients downstream of the nucleus under shear stress. Therefore, we hope that our future simulation model together with experiments will confirm.

Also, the MATLAB algorithm used to analyze the orientation of the MTOC in relation to the nucleus can be improved to detect the MTOC-nuclear pairs instead of the manual picking to eliminate human error and lower the time needed for analysis.

## LIST OF REFERENCES

1. A. E. Medvedev, V. I. Samsonov, and V. M. Fomin, “Rational structure of blood vessels,” *Journal of Applied Mechanics and Technical Physics*, vol. 47, no. 3, pp. 324–329, 2006.
2. J. Eble and S. Niland, “The extracellular matrix of blood vessels,” *Current pharmaceutical design*, vol. 15, pp. 1385–1400, Feb. 2009.
3. A. Krüger-Genge, A. Blocki, R.-P. Franke, and F. Jung, “Vascular endothelial cell biology: An update,” *International Journal of Molecular Sciences*, vol. 20, no. 18, 2019.
4. R. Mazurek, J. Dave, R. R. Chandran, A. Misra, A. Sheikh, and D. Greif, “Vascular cells in blood vessel wall development and disease,” in Oct. 2016, vol. 78.
5. M. W. Majesky, X. R. Dong, V. Hoglund, W. M. Mahoney, and G. Daum, “The adventitia,” *Arteriosclerosis, Thrombosis, and Vascular Biology*, vol. 31, no. 7, pp. 1530–1539, 2011.
6. A. Barakat and D. Lieu, “Differential responsiveness of vascular endothelial cells to different types of fluid mechanical shear stress,” *Cell biochemistry and biophysics*, vol. 38, pp. 323–343, Feb. 2003.
7. Y.-S. J. Li, J. H. Haga, and S. Chien, “Molecular basis of the effects of shear stress on vascular endothelial cells,” English, *Journal of Biomechanics*, vol. 38, no. 10, pp. 1949–1971, 2005.
8. J.-J. Chiu and S. Chien, “Effects of disturbed flow on vascular endothelium: Pathophysiological basis and clinical perspectives,” *Physiological Reviews*, vol. 91, no. 1, pp. 327–387, 2011.
9. Y. Jiang and J. Y. Ji, “Expression of nuclear lamin proteins in endothelial cells is sensitive to cell passage and fluid shear stress,” *Cellular and Molecular Bioengineering*, vol. 11, no. 1, pp. 53–64, 2018.
10. S. Chatterjee, “Endothelial mechanotransduction, redox signaling and the regulation of vascular inflammatory pathways,” *Frontiers in Physiology*, vol. 9, 2018.
11. M. K. Fitts, D. B. Pike, K. Anderson, and Y.-T. Shiu, “Hemodynamic shear stress and endothelial dysfunction in hemodialysis access,” *The open urology & nephrology journal*, vol. 7, pp. 33–44, 2014.
12. B. D. Johnson, K. J. Mather, and J. P. Wallace, “Mechanotransduction of shear in the endothelium: Basic studies and clinical implications,” *Vascular Medicine*, vol. 16, no. 5, pp. 365–377, 2011.

13. J. Abe and B. C. Berk, “Novel mechanisms of endothelial mechanotransduction,” *Arteriosclerosis, Thrombosis, and Vascular Biology*, vol. 34, no. 11, pp. 2378–2386, 2014.
14. J. Ando and K. Yamamoto, “Effects of shear stress and stretch on endothelial function,” *Antioxidants & Redox Signaling*, vol. 15, no. 5, pp. 1389–1403, 2011.
15. Y. Jiang, N. Witt, and J. Y. Ji, “Passage dependent changes in nuclear and cytoskeleton structures of endothelial cells under laminar shear stress or cyclic stretch,” *International Journal of Scientific Reports*, vol. 7, no. 7, pp. 327–339, 2021.
16. S. Chien, “Mechanotransduction and endothelial cell homeostasis: The wisdom of the cell,” *American Journal of Physiology-Heart and Circulatory Physiology*, vol. 292, no. 3, H1209–H1224, 2007.
17. A. Malek and S. Izumo, “Mechanism of endothelial cell shape change and cytoskeletal remodeling in response to fluid shear stress,” *Journal of Cell Science*, vol. 109, no. 4, pp. 713–726, Apr. 1996.
18. S. Li, N. F. Huang, and S. Hsu, “Mechanotransduction in endothelial cell migration,” *Journal of Cellular Biochemistry*, vol. 96, no. 6, pp. 1110–1126, 2005.
19. E. Tkachenko, E. Gutierrez, S. K. Saikin, P. Fogelstrand, C. Kim, A. Groisman, and M. H. Ginsberg, “The nucleus of endothelial cell as a sensor of blood flow direction,” *Biology Open*, vol. 2, no. 10, pp. 1007–1012, Aug. 2013.
20. G. G. Gundersen and H. J. Worman, “Nuclear Positioning,” *Cell*, vol. 152, no. 6, pp. 1376–1389, 2013.
21. C. M. Hale, W.-C. Chen, S. B. Khatau, B. R. Daniels, J. S. H. Lee, and D. Wirtz, “SMRT analysis of MTOC and nuclear positioning reveals the role of EB1 and LIC1 in single-cell polarization,” *Journal of Cell Science*, vol. 124, no. 24, pp. 4267–4285, Dec. 2011.
22. A. F. Palazzo, H. L. Joseph, Y.-J. Chen, D. L. Dujardin, A. S. Alberts, K. Pfister, R. B. Vallee, and G. G. Gundersen, “Cdc42, dynein, and dynactin regulate mtoc reorientation independent of rho-regulated microtubule stabilization,” *Current Biology*, vol. 11, no. 19, pp. 1536–1541, 2001.
23. M. Maninová, M. P. Iwanicki, and T. Vomastek, “Emerging role for nuclear rotation and orientation in cell migration,” *Cell Adhesion & Migration*, vol. 8, no. 1, pp. 42–48, 2014.

24. K. B. Vartanian, S. J. Kirkpatrick, S. R. Hanson, and M. T. Hinds, "Endothelial cell cytoskeletal alignment independent of fluid shear stress on micropatterned surfaces," *Biochemical and Biophysical Research Communications*, vol. 371, no. 4, pp. 787–792, 2008.
25. J. T. Morgan, E. R. Pfeiffer, T. L. Thirkill, P. Kumar, G. Peng, H. N. Fridolfsson, G. C. Douglas, D. A. Starr, and A. I. Barakat, "Nesprin-3 regulates endothelial cell morphology, perinuclear cytoskeletal architecture, and flow-induced polarization," *Molecular Biology of the Cell*, vol. 22, no. 22, pp. 4324–4334, 2011.
26. A. Dobrzynska, S. Gonzalo, C. Shanahan, and P. Askjaer, "The nuclear lamina in health and disease," *Nucleus*, vol. 7, no. 3, pp. 233–248, 2016.
27. A. Mattout, T. Dechat, S. Adam, R. Goldman, and Y. Gruenbaum, "Nuclear lamins, diseases and aging," *Current opinion in cell biology*, vol. 18, pp. 335–341, Jul. 2006.
28. F. Donnalaja, F. Carnevali, E. Jacchetti, and M. Raimondi, "Lamin a/c mechanotransduction in laminopathies," *Cells*, vol. 9, p. 1306, 2020.
29. R. Kreienkamp and S. Gonzalo, "Hutchinson-gilford progeria syndrome: Challenges at bench and bedside," in *Biochemistry and Cell Biology of Ageing: Part II Clinical Science*, J. R. Harris and V. I. Korolchuk, Eds. Singapore: Springer Singapore, 2019, pp. 435–451.
30. P. Kim, J. Luu, P. Heizer, Y. Tu, T. Weston, N. Chen, C. Lim, R. Li, P.-Y. Lin, J. Dunn, D. Hodzic, S. Young, and L. Fong, "Disrupting the linc complex in smooth muscle cells reduces aortic disease in a mouse model of hutchinson-gilford progeria syndrome," *Science Translational Medicine*, vol. 10, no. 460, 2018.
31. K. Harhour, D. Frankel, C. Bartoli, P. Roll, A. D. Sandre-Giovannoli, and N. Lévy, "An overview of treatment strategies for hutchinson-gilford progeria syndrome," *Nucleus*, vol. 9, no. 1, pp. 265–276, 2018.
32. Y. Jiang and J. Y. Ji, "Understanding lamin proteins and their roles in aging and cardiovascular diseases," *Life Sciences*, vol. 212, pp. 20–29, 2018.
33. J. Hah and D.-H. Kim, "Deciphering nuclear mechanobiology in laminopathy," *Cells*, vol. 8, no. 3, 2019.
34. N. Bonello-Palot, S. Simoncini, S. Robert, P. Bourgeois, F. Sabatier, N. Lévy, F. Dignat-George, and C. Badens, "Prelamin a accumulation in endothelial cells induces premature senescence and functional impairment.," *Atherosclerosis*, vol. 237, no. 1, pp. 45–52, 2014.
35. A. Singh and A. Gupta, *Basics of Cell Biology and Biotechnology*. Laxmi Publications Pvt Ltd, 2018, vol. First edition.

36. C. Lloy, “Finite Element Modelling of Living Cells,” M.S. thesis, University of Edinburgh, the Netherlands, 2014.
37. C. Lim, E. Zhou, and S. Quek, “Mechanical models for living cells—a review,” *Journal of biomechanics*, vol. 39, pp. 195–216, Feb. 2006.
38. V. Lulevich, C. C. Zimmer, H.-s. Hong, L.-w. Jin, G.-y. Liu, and G. W. Flynn, “Single-cell mechanics provides a sensitive and quantitative means for probing amyloid- $\beta$  peptide and neuronal cell interactions,” *Proceedings of the National Academy of Sciences of the United States of America*, vol. 107, no. 31, pp. 13 872–13 877, 2010.
39. R. D. Kamm, A. K. McVittie, and M. Bathe, “On the role of continuum models in mechanobiology,” *ASME Applied Mechanics*, vol. 242, pp. 1–12, 2000.
40. B. Alberts, D. Bray, K. Hopkin, A. Johnson, J. Lewis, M. Raff, K. Roberts, and P. Walter, *Essential Cell Biology*. Garland Science, 2014, vol. Fourth edition.
41. N. Caille, O. Thoumine, Y. Tardy, and J.-J. Meister, “Contribution of the nucleus to the mechanical properties of endothelial cells,” *Journal of biomechanics*, vol. 35, pp. 177–187, 2002.
42. F. Guilak, J. Tedrow, and R. Burgkart, “Viscoelastic properties of the cell nucleus,” *Biochemical and biophysical research communications*, vol. 269, pp. 781–786, 2000.
43. H. Lodish, A. Berk, P. Matsudaira, C. A. Kaiser, M. Krieger, M. P. Scott, L. Zipursky, and J. Darnell, *Molecular Cell Biology*. W.H. Freeman and Company: New York, NY, USA, 2005, vol. Fifth edition.
44. R. D. Mullins and D. A. Fletcher, “Cell mechanics and the cytoskeleton,” *Nature*, vol. 463, pp. 485–492, 2010.
45. A. Shpilman, D. Boikiy, M. Polyakova, D. Kudenko, A. Burakov, and E. Nadezhdina, “Deep learning of cell classification using microscope images of intracellular microtubule networks,” 2020.
46. J. McGarry and P. Prendergast, “A three-dimensional finite element model of an adherent eukaryotic cell,” *European Cells and Materials*, vol. 7, pp. 27–34, 2004.
47. Y. Bansod, T. Matsumoto, N. Kazuaki, and J. Bursa, “A finite element bendo-tensegrity model of eukaryotic cell,” *Journal of Biomechanical Engineering*, vol. 140, Apr. 2018.
48. H. Huang, C. Dai, H. Shen, M. Gu, Y. Wang, J. Liu, L. Chen, and L. Sun, “Recent advances on the model, measurement technique, and application of single cell mechanics,” *International Journal of Molecular Sciences*, vol. 21, no. 17, 2020.

49. D. E. Ingber, "Tensegrity I. Cell structure and hierarchical systems biology," *Journal of Cell Science*, vol. 116, no. 7, pp. 1157–1173, Apr. 2003.
50. D. E. Ingber, N. Wang, and D. Stamenović, "Tensegrity, cellular biophysics, and the mechanics of living systems.," *Reports on progress in physics. Physical Society (Great Britain)*, vol. 77, no. 4, p. 046 603, Apr. 2014.
51. N. Wang and D. Stamenović, "Contribution of intermediate filaments to cell stiffness, stiffening, and growth," *American Journal of Physiology-Cell Physiology*, vol. 279, no. 1, pp. C188–C194, 2000.
52. S. Barreto, C. H. Clausen, C. M. Perrault, D. A. Fletcher, and D. Lacroix, "A multi-structural single cell model of force-induced interactions of cytoskeletal components," *Biomaterials*, vol. 34, no. 26, pp. 6119–6126, 2013.
53. S. Barreto, C. M. Perrault, and D. Lacroix, "Structural finite element analysis to explain cell mechanics variability," *Journal of the Mechanical Behavior of Biomedical Materials*, vol. 38, pp. 219–231, 2014.
54. J. G. McGarry, J. Klein-Nulend, M. G. Mullender, and P. J. Prendergast, "A comparison of strain and fluid shear stress in stimulating bone cell responses—a computational and experimental study.," *The FASEB Journal*, vol. 19, no. 3, pp. 1–22, 2005.
55. *ANSYS Mechanical APDL Element Reference*, Release 15.0. ANSYS, Inc., 2013.
56. Y. Jiang, "Mechano-sensitivity of nuclear lamin proteins in endothelial cells," M.S. thesis, Purdue University, Indianapolis, Indiana, 2016.
57. R. W. Fox, A. T. McDonald, and P. J. Pritchard, *Introduction to Fluid Mechanics*. John Wiley & Sons, Inc., 2003, vol. Sixth edition.
58. R. Thavarajah, V. Mudimbaimannar, J. Elizabeth, U. Rao, and K. Ranganathan, "Chemical and physical basics of routine formaldehyde fixation," *Journal of oral and maxillo-facial pathology : JOMFP*, vol. 16, pp. 400–405, Sep. 2012.
59. Y. Xiao and S. N. Isaacs, "Enzyme-linked immunosorbent assay (elisa) and blocking with bovine serum albumin (bsa) - not all bsas are alike," *Journal of immunological methods*, vol. 384, no. 1-2, pp. 148–151, 2012.
60. S. McCue, D. Dajnowiec, F. Xu, M. Zhang, M. R. Jackson, and B. L. Langille, "Shear stress regulates forward and reverse planar cell polarity of vascular endothelium in vivo and in vitro," *Circulation Research*, vol. 98, no. 7, pp. 939–946, 2006.

61. E. Tzima, W. B. Kiosses, M. A. del Pozo, and M. A. Schwartz, “Localized cdc42 activation, detected using a novel assay, mediates microtubule organizing center positioning in endothelial cells in response to fluid shear stress,” *Journal of Biological Chemistry*, vol. 278, no. 33, pp. 31 020–31 023, 2003.
62. B. S. Dragt, E. L. van Agtmaal, B. de Laat, and J. Voorberg, “Effect of laminar shear stress on the distribution of weibel-palade bodies in endothelial cells,” *Thrombosis Research*, vol. 130, no. 5, pp. 741–745, 2012.